

Fibrin-targeting immunotherapy protects against neuroinflammation and neurodegeneration

Jae Kyu Ryu¹, Victoria A. Rafalski^{1,13}, Anke Meyer-Franke^{1,13}, Ryan A. Adams², Suresh B. Poda³, Pamela E. Rios Coronado¹, Lars Østergaard Pedersen⁴, Veena Menon³, Kim M. Baeten¹, Shoana L. Sikorski², Catherine Bedard¹, Kristina Hanspers¹, Sophia Bardehle¹, Andrew S. Mendiola¹, Dimitrios Davalos^{1,12}, Michael R. Machado¹, Justin P. Chan¹, Ioanna Plastira^{1,5}, Mark A. Petersen^{1,6}, Samuel J. Pfaff⁷, Kenny K. Ang⁷, Kenneth K. Hallenbeck⁷, Catriona Syme¹, Hiroyuki Hakozaiki⁸, Mark H. Ellisman^{8,9}, Raymond A. Swanson^{10,11}, Scott S. Zamvil¹¹, Michelle R. Arkin⁷, Stevin H. Zorn³, Alexander R. Pico¹, Lennart Mucke^{1,11}, Stephen B. Freedman¹, Jeffrey B. Stavenhagen⁴, Robert B. Nelson³ and Katerina Akassoglou^{1,2,11*}

Activation of innate immunity and deposition of blood-derived fibrin in the central nervous system (CNS) occur in autoimmune and neurodegenerative diseases, including multiple sclerosis (MS) and Alzheimer's disease (AD). However, the mechanisms that link disruption of the blood-brain barrier (BBB) to neurodegeneration are poorly understood, and exploration of fibrin as a therapeutic target has been limited by its beneficial clotting functions. Here we report the generation of monoclonal antibody 5B8, targeted against the cryptic fibrin epitope $\gamma_{377-395}$, to selectively inhibit fibrin-induced inflammation and oxidative stress without interfering with clotting. 5B8 suppressed fibrin-induced nicotinamide adenine dinucleotide phosphate (NADPH) oxidase activation and the expression of proinflammatory genes. In animal models of MS and AD, 5B8 entered the CNS and bound to parenchymal fibrin, and its therapeutic administration reduced the activation of innate immunity and neurodegeneration. Thus, fibrin-targeting immunotherapy inhibited autoimmunity- and amyloid-driven neurotoxicity and might have clinical benefit without globally suppressing innate immunity or interfering with coagulation in diverse neurological diseases.

Activation of innate immunity is a key feature of neurological diseases with different etiologies, including autoimmune and neurodegenerative CNS diseases¹. Increasing evidence indicates that pathogenic activation of CNS innate immunity contributes to neuronal damage and modulates the onset and progression of neurodegenerative diseases². Oxidative injury and release of free radicals have been proposed as common mechanisms for innate immunity-driven neurodegeneration and demyelination in MS and AD³⁻⁶. Chronic activation of innate immunity and oxidative injury are key elements that drive neurodegeneration in both relapsing-remitting MS and progressive MS^{3,7,8}. In progressive MS, there is robust microglial activation, oxidative stress and neurodegeneration^{3,8,9}. Pathogenic activation of innate immunity contributes to oxidative stress and cognitive decline in AD⁵. Little is known about the pathogenic signals that activate innate immune cells toward neurotoxic phenotypes. Understanding the mechanisms of the activation of CNS innate immunity is essential for deciphering how neuroinflammation contributes to neuronal damage and for designing treatments for the selective suppression of pathogenic functions of innate immunity.

The activation of innate immunity, disruption of the BBB and deposition of fibrin are intimately linked in neurological diseases^{10,11}. The blood-coagulation factor fibrinogen extravasates into the CNS parenchyma after disruption of the BBB and is converted into insoluble fibrin, a key proinflammatory matrix that activates innate immune responses^{11,12}. The conversion of fibrinogen into fibrin exposes amino acids 377–395 in the fibrinogen γ -chain ($\gamma_{377-395}$) that bind to the CD11b I-domain of the CD11b-CD18 integrin receptor (also known as Mac-1, complement receptor 3 (CR3), or $\alpha_M\beta_2$) and induces the activation of microglia and macrophages¹³⁻¹⁶. Fibrin is deposited in AD and MS lesions at sites of microglial activation and macrophage infiltration (reviewed in ref. ¹¹). Fibrin is detected in progressive MS and in active and chronic lesions (reviewed in ref. ¹¹). In progressive MS, deposition of fibrin in the cortex correlates with neuronal loss and inhibition of fibrinolysis¹⁷. Disruption of the BBB and deposition of fibrin also occur early in MS and precede demyelination^{18,19}. Fibrinogen has been proposed as a cerebrospinal fluid and plasma biomarker for AD and mild cognitive impairment, and increased concentrations of fibrinogen are considered a predictor of brain atrophy in AD (reviewed in refs ^{11,20}). Depletion of fibrin

¹Gladstone Institutes, San Francisco, CA, USA. ²Department of Pharmacology, University of California, San Diego, La Jolla, CA, USA. ³Lundbeck Research USA, Paramus, NJ, USA. ⁴H. Lundbeck A/S, Copenhagen, Denmark. ⁵Institute of Molecular Biology and Biochemistry, Medical University Graz, Graz, Austria. ⁶Division of Neonatology, Department of Pediatrics, University of California, San Francisco, San Francisco, CA, USA. ⁷Small Molecule Discovery Center, Department of Pharmaceutical Chemistry, University of California, San Francisco, San Francisco, CA, USA. ⁸National Center for Microscopy and Imaging Research, University of California, San Diego, La Jolla, CA, USA. ⁹Department of Neurosciences, University of California, San Diego, La Jolla, CA, USA. ¹⁰Neurology Service, San Francisco Veteran Affairs Medical Center, San Francisco, CA, USA. ¹¹Department of Neurology, University of California, San Francisco, San Francisco, CA, USA. ¹²Present address: Department of Neurosciences, Lerner Research Institute, Cleveland Clinic Foundation, Cleveland, OH, USA. ¹³These authors contributed equally: Victoria A. Rafalski, Anke Meyer-Franke. *e-mail: kakassoglou@gladstone.ucsf.edu

either genetically in fibrinogen-deficient mice or by anticoagulants decreases neuroinflammation, demyelination and axonal damage in animal models of MS and reduces the activation of microglia, damage to white matter and cognitive decline in animal models of AD (reviewed in ref. ¹¹). Fibrin induces rapid and sustained microglial responses and infiltration of macrophages into the CNS^{15,16}. Although increased disruption of the BBB and deposition of fibrin correlate with neurodegeneration, the molecular links between the leakage of blood into the CNS and neuronal damage are poorly understood. Furthermore, whether and how fibrin-induced activation of innate immunity is neurotoxic remains largely unknown.

Here we report an unanticipated role for fibrin as an activator of the NADPH oxidase complex that induced the release of reactive oxygen species (ROS) and innate immunity-driven neurotoxicity in autoimmunity- and amyloid-driven neurodegeneration. Although activation of innate immunity is an attractive candidate for therapeutic intervention, selective therapies that inhibit the neurotoxic effects of innate immune responses are not widely available. By targeting the cryptic fibrin epitope $\gamma_{377-395}$, we developed the first, to our knowledge, fibrin-targeting immunotherapy (monoclonal antibody 5B8) that selectively targets the inflammatory form of fibrin without interfering with clotting or the activation of innate immune cells by other ligands, such as lipopolysaccharide (LPS). 5B8 selectively bound to fibrin, but not to soluble fibrinogen, and inhibited binding of fibrin to CR3 without interfering with fibrin polymerization, *in vivo* clotting time or activated partial thromboplastin time (aPTT) in human plasma. 5B8 reduced the activation of NADPH oxidase, the release of ROS, the activation of microglia and neurodegeneration in animal models of MS and AD. These studies identify fibrin as a blood-derived signal that activates NADPH oxidase to promote innate immunity-driven neurotoxicity and identify fibrin-targeted immunotherapy as a novel therapeutic strategy that suppresses innate immunity-driven neurodegeneration at sites of increased vascular permeability without interfering with clotting or globally suppressing innate immunity.

Results

Design of fibrin-targeting immunotherapy. The carboxyl terminus of the fibrinogen γ -chain contains two distinct non-overlapping sites at $\gamma_{400-411}$ and $\gamma_{377-395}$, which mediate platelet engagement and inflammation, respectively (Fig. 1a). Peptide $\gamma_{400-411}$ is the binding site for the platelet integrin receptor $\alpha_{IIb}\beta_3$ and is required for platelet aggregation. Peptide $\gamma_{377-395}$ is the binding site for the CD11b I-domain of CD11b-CD18¹⁴ and is required for fibrin-induced activation of microglia and macrophages^{13,15,16}. The binding site $\gamma_{377-395}$ is considered 'cryptic' in the soluble fibrinogen molecule and is exposed only after the conversion of fibrinogen to insoluble fibrin¹⁴ (Fig. 1a). We hypothesized that monoclonal antibodies to $\gamma_{377-395}$ would selectively recognize fibrin and inhibit fibrin's interaction with the CD11b I-domain without affecting blood coagulation. To control for CD11b I-domain-binding specificity, we also generated mouse monoclonal antibodies to the fibrin epitope $\gamma_{190-202}$, which is also cryptic but is not required for binding to the CD11b I-domain¹⁴. Using a streamlined screening strategy, we selected monoclonal antibodies that selectively bound fibrin and inhibited the activation of microglia (Supplementary Fig. 1a). Antibodies 5B8, 4E11 and 4F1 had the greatest selectivity and specificity for $\gamma_{377-395}$, while antibody 1E3, directed against $\gamma_{190-202}$, did not bind $\gamma_{377-395}$, as expected (Fig. 1b and Supplementary Fig. 1b). To discriminate between fibrinogen and fibrin in biochemical and cellular assays, we developed an *in vitro* fibrin substrate that bound to a recombinant CD11b I-domain more strongly than fibrinogen did (Supplementary Fig. 1c), which suggested exposure of the $\gamma_{377-395}$ epitope *in vitro*. All antibodies to cryptic epitopes bound with higher affinity to fibrin than to fibrinogen; among antibodies targeting $\gamma_{377-395}$, 5B8 bound fibrin to the greatest degree, with minimal binding to soluble fibrinogen

(Fig. 1c and Supplementary Fig. 1d). Competitive binding assays showed that 5B8 bound to human and mouse $\gamma_{377-395}$ peptides but not to $\gamma_{190-202}$ peptide (Supplementary Fig. 1e). 5B8 inhibited binding of the CD11b I-domain to fibrin (Fig. 1d), which suggested that 5B8 interfered with the ligand-receptor interaction.

Fibrin activates microglia, as indicated by morphological activation characterized by an increase in cell size that is also associated with gene-expression changes^{13,16}. An assay of morphological activation, combined with automated quantification, was suitable for an unbiased and rapid comparison of multiple fibrin-targeting antibody clones in primary microglial cultures. Notably, among all antibodies generated against cryptic epitopes, only antibodies to $\gamma_{377-395}$ inhibited fibrin-induced morphological activation of microglia; the greatest inhibition (~87%) was by 5B8 (Supplementary Fig. 2a). Antibody 1E3, directed against $\gamma_{190-202}$, also bound fibrin but did not inhibit microglial activation (Supplementary Fig. 2a), suggesting that inhibition of fibrin's proinflammatory functions depends on targeting $\gamma_{377-395}$. The F(ab) fragment of 5B8 also inhibited fibrin-induced microglial activation (Supplementary Fig. 2b). 5B8 inhibited fibrin-induced morphological microglial activation in a concentration-dependent manner and reduced the expression of genes encoding proinflammatory molecules (Fig. 1e and Supplementary Fig. 2c,d). The isotype-matched control antibody IgG2b, with endotoxin concentrations of <0.002 EU/ μ g (Supplementary Fig. 2e), was used as control for all experiments in the study. 5B8 did not alter the polymerization of fibrinogen into fibrin, did not inhibit the aPTT in human plasma and had no effect on the clotting time of mouse plasma *in vivo* (Fig. 1f-h). ~80% of 5B8 was recovered 5 d after a single intraperitoneal injection into healthy wild-type mice (Supplementary Fig. 2f), which suggested that 5B8's preferential binding to fibrin and minimal binding to soluble fibrinogen resulted in a minimal sink effect.

In microglia and macrophages, fibrin induces the expression of genes encoding proinflammatory molecules associated with immune responses and cell recruitment¹⁶. In bone marrow-derived macrophages (BMDMs), 5B8 reduced the fibrin-induced transcriptional activation of genes encoding molecules related to the migration of immune cells, adhesion, inflammatory responses, regulation of T cell proliferation and chemotaxis, as shown by whole-genome microarray and gene-ontology (GO) analysis (Fig. 2a-c). A heat map of the 20 most-affected transcripts showed that 5B8 inhibited the fibrin-induced transcription of a group of genes encoding molecules that regulate innate and/or adaptive immune responses (Fig. 2c). The reduction in the expression of *Ccl24*, *Tnfs18*, *Il12b*, *Cxcl3* and *Ifng* (which encode proinflammatory molecules) by 5B8 was confirmed by quantitative RT-PCR (Fig. 2d). 5B8 did not affect the LPS-induced expression of genes encoding proinflammatory molecules (Fig. 2e), which suggested that the suppression of the activation of innate immunity by 5B8 might have been selective for fibrin. Furthermore, 5B8 or its F(ab) fragment alone inhibited microglial activation and the expression of chemokine-encoding genes in fibrinogen-induced encephalomyelitis (Supplementary Fig. 3), an acute neuroinflammatory model that results from fibrin-induced microglial activation¹⁶. Thus, we had devised a paradigm for the development of a fibrin epitope-specific immunotherapy. The result was 5B8, a highly selective monoclonal antibody that blocked fibrin-induced, CD11b-mediated activation of innate immunity without affecting fibrin polymerization, *in vivo* clotting time or aPTT in human plasma.

Fibrin induces NADPH oxidase-mediated neurodegeneration.

A consequence of the activation of innate immunity in CNS auto-immune and neurodegenerative diseases is neurotoxicity; its successful treatment remains a major unmet clinical need. Intriguingly, fibrin induced the expression of several genes encoding molecules that regulate oxidative stress and the release of ROS (Fig. 3a) and

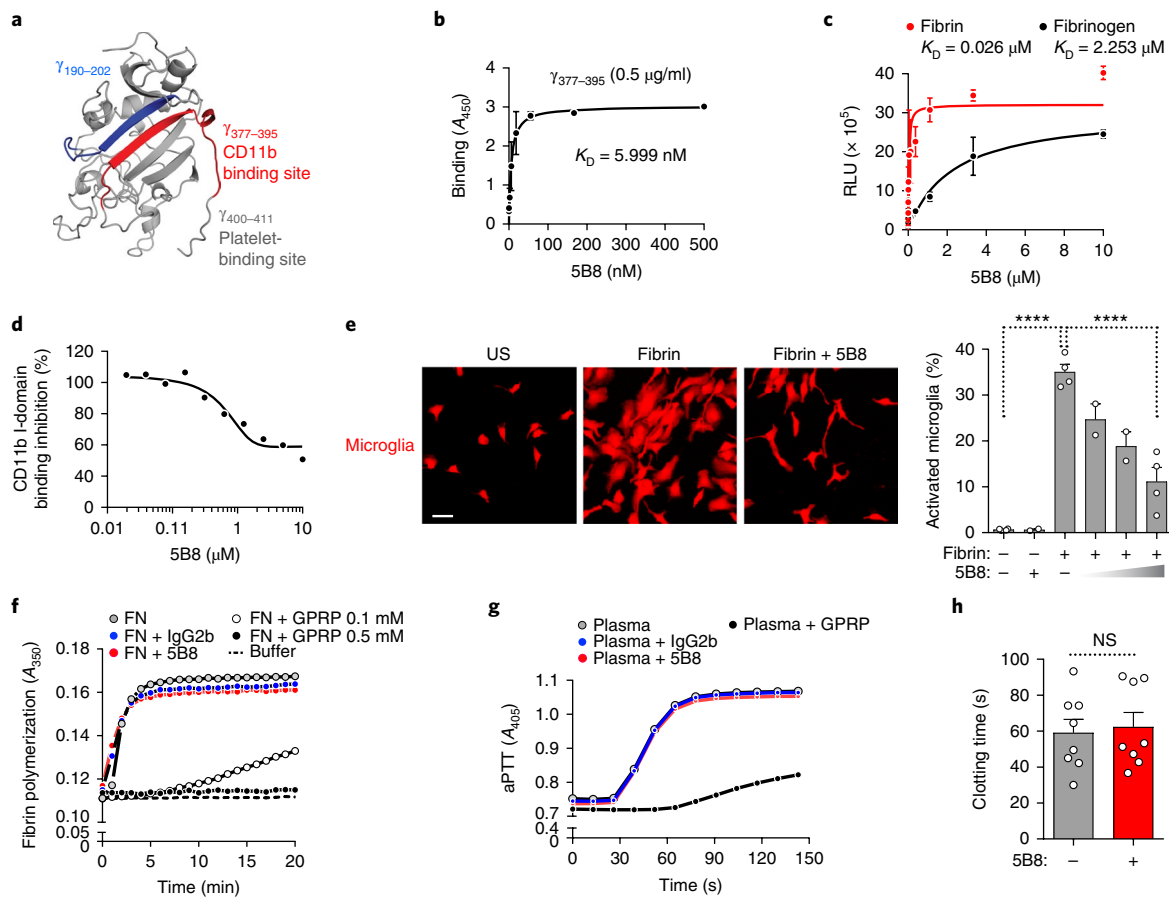


Fig. 1 | Generation and characterization of monoclonal antibody 5B8, which targets the fibrin epitope $\gamma_{377-395}$. **a**, Structural map of the carboxy-terminal γ -chain of fibrinogen, showing the cryptic epitope $\gamma_{377-395}$ (red), which binds to the CD11b I-domain, as well as epitopes $\gamma_{190-202}$ (blue) and $\gamma_{400-411}$ (gray). **b**, ELISA of the binding of 5B8 to $\gamma_{377-395}$, presented as absorbance at 450 nm (A_{450}), plus the dissociation constant (K_D). Data are from four independent experiments (mean \pm s.e.m.). **c**, ELISA of the binding of 5B8 to fibrin and fibrinogen (key), presented as relative chemiluminescent light units (RLU). Data are from three independent experiments (mean \pm s.e.m.). **d**, Competitive ELISA of 5B8 versus the CD11b I-domain for binding to fibrin. Data are from one experiment. **e**, Microscopy (left) of microglia left unstimulated (US) or stimulated with fibrin alone or in the presence of 5B8 (40 $\mu\text{g}/\text{ml}$) (above images), and quantification of microglial activation assessed as increased cell size (right) at 48 h after treatment with various combinations (below plots) of the presence (+) or absence (-) of fibrin and 5B8 (40 $\mu\text{g}/\text{ml}$ (+) or 10, 20 or 40 $\mu\text{g}/\text{ml}$ (wedge)). Scale bar (left), 10 μm . Each symbol (right) represents an independent experiment. Data are from four independent experiments (untreated, fibrin, fibrin + 5B8 (40 $\mu\text{g}/\text{ml}$)) and two independent experiments (fibrin + 5B8 (10, 20 $\mu\text{g}/\text{ml}$)) with similar results by manual and automated quantification (mean \pm s.e.m.). **** $P < 0.0001$ (one-way analysis of variance (ANOVA) with Sidak's multiple comparisons test). **f**, In vitro fibrin polymerization in the presence of buffer or fibrinogen (FN) alone or with 5B8, IgG2b or various concentrations of the fibrin polymerization inhibitor (positive control) GPRP (key). Data are representative of two independent experiments with similar results. **g**, aPTT assay of human plasma in the presence or absence of 5B8, IgG2b or GPRP (key). Data are representative of two independent experiments with similar results. **h**, In vivo clotting time of blood from mice given injection of 5B8 (+) or not (-). Each symbol represents an individual mouse. Data are from $n = 8$ mice per treatment (mean \pm s.e.m.). NS, not significant ($P = 0.7768$) (two-tailed Mann-Whitney test).

that are linked to neurotoxicity^{7,21}. *Ncf4*, which encodes the p40^{phox} subunit of the NADPH oxidase Nox2 complex, was among the genes most upregulated by fibrin (Fig. 3a). NADPH oxidase is a multicomponent enzyme system that is upregulated in human MS²² and AD²³. Increased activation of NADPH oxidase and oxidative stress are common mechanisms of neurodegeneration in diseases with fibrin deposition, including MS, AD, stroke, traumatic brain injury and brain aging^{6,24,25}. Intriguingly, fibrin increased protein expression of the Nox2 component gp91^{phox}, phosphorylation of p40^{phox} and NADPH oxidase activity; these increases were all reduced when macrophages were treated with 5B8 (Fig. 3b,c). Treatment with 5B8 inhibited the fibrin-induced release of ROS in both mouse macrophages and human macrophages (Fig. 3d,e). The fibrin-induced generation of ROS was reduced in BMDMs when the p47^{phox} subunit of NADPH oxidase was ablated genetically and when NADPH oxidase or CD11b was inhibited by treatment

with apocynin or the M1/70 antibody to CD11b, respectively (Fig. 3f,g and Supplementary Fig. 4a). In the culture conditions assessed, stimulation with fibrin or treatment with antibodies did not affect BMDM density (Supplementary Fig. 4b). In a co-culture of cortical neurons and macrophages, which recapitulates the non-cell-autonomous degeneration of CNS neurons, fibrin-primed macrophages induced significant loss of MAP-2⁺ neurons and increased the fragmentation and blebbing of neurites (Fig. 3h). Notably, 5B8 effectively blocked this pathogenic cascade (Fig. 3h). These results suggested that fibrin caused neurotoxicity via a causal chain that involved CD11b-mediated activation of innate immune cells and increased ROS production by NADPH oxidase.

Fibrin-targeting immunotherapy protects EAE mice from axonal damage. Evidence from human MS has underscored the contributions of fibrin, innate immunity and oxidative stress to the onset

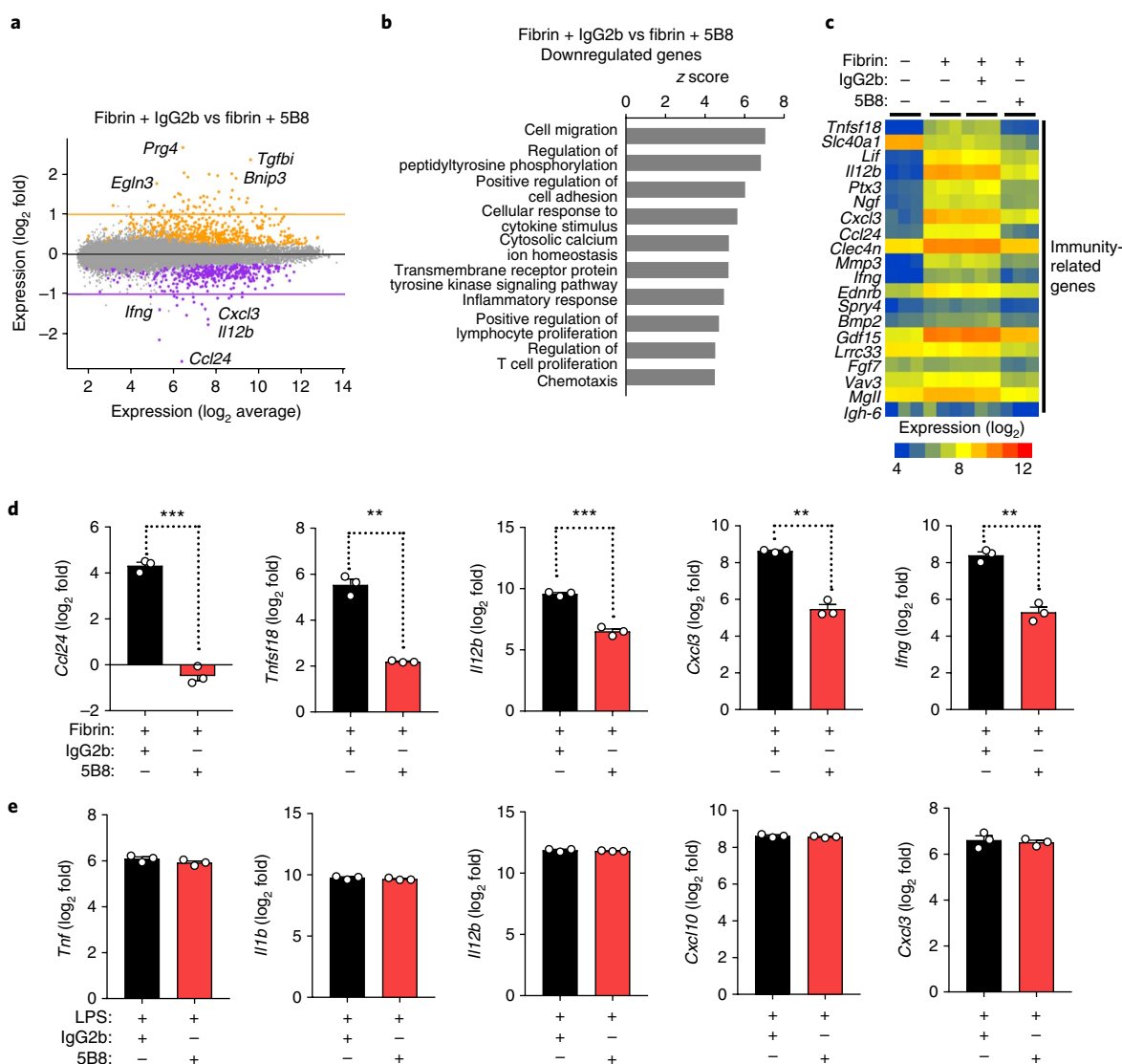


Fig. 2 | Changes in gene expression induced by the treatment of fibrin-stimulated BMDMs with 5B8. **a**, Whole-genome microarray analysis of BMDMs stimulated for 6 h with fibrin and 5B8 or IgG2b (above plot), presented as an MA plot of the ratio of expression in 5B8-treated BMDMs relative to that in IgG2b-treated BMDMs (log₂ fold values) (M) versus mean average expression of each gene (A), showing genes whose expression was significantly increased (orange) or decreased (purple) by 5B8 or not (gray); horizontal lines indicate no change in expression (middle) or delimit a change in expression of 1-fold to -1-fold. Selected genes among the top 10 downregulated or upregulated are labeled. Data are from three independent experiments. $P < 0.001$ (two-tailed, raw; moderated t -test). **b**, GO-Elite analysis of transcripts in BMDMs treated as in **a** (above plot), identifying the top ten biological processes (left margin) with the most significantly downregulated transcripts in 5B8-treated BMDMs relative to their expression in IgG2b-treated BMDMs (z-score > 2.0 ; $P < 0.05$). **c**, Whole-genome microarray analysis of the expression (key below) of various immunity-related genes (left margin) in BMDMs treated with various combinations (grid above plot) of fibrin, 5B8 and IgG2, identifying the top 20 most significantly downregulated transcripts in fibrin-stimulated BMDMs treated with 5B8. Data are from three independent experiments. Each column represents one sample from each experiment. **d**, qRT-PCR analysis of transcripts from genes encoding proinflammatory molecules in BMDMs treated as in **c** (grid below plot), presented as expression in fibrin-stimulated BMDMs treated with 5B8 relative to that in those treated with IgG2b (log₂ fold values). Each symbol represents an individual experiment. Data are from three independent experiments (mean + s.e.m.). $^{**}P = 0.0052$ (*Tnfsf18*), 0.0050 (*Cxcl3*) or 0.0015 (*Ifng*), and $^{***}P = 0.0001$ (*Ccl24*) or 0.0010 (*Il12b*) (unpaired two-tailed t -test with Welch's correction). **e**, qRT-PCR analysis of BMDMs treated with various combinations (grid below plot) of LPS, IgG2b and 5B8, presented as expression in LPS-stimulated BMDMs treated with 5B8 relative to that in those treated with IgG2b (log₂ fold values). Each symbol represents an individual experiment. Data are from three independent experiments (mean + s.e.m.). P values, not significant (unpaired two-tailed t -test with Welch's correction).

and progression of disease and disability^{3,8,9,19,22,26}. To investigate the role of fibrin in neurotoxicity in vivo, we first assessed the effects of 5B8 in three models of experimental autoimmune encephalomyelitis (EAE) that simulate key aspects of MS: relapsing–remitting EAE induced by the epitope of amino acids 139–151 of proteolipid protein (PLP) ('PLP_{139–151} EAE'); chronic EAE induced by the epitope

of amino acids 35–55 of myelin oligodendrocyte glycoprotein (MOG) ('MOG_{35–55} EAE'); and adoptive transfer of CD4⁺ T cells differentiated under conditions that polarize cells into the T_H1 subset of helper T cells. Given prophylactically, 5B8 reduced neurological signs in all three models relative to the neurological signs of groups treated with the IgG2b isotype-matched control antibody (Fig. 4a).

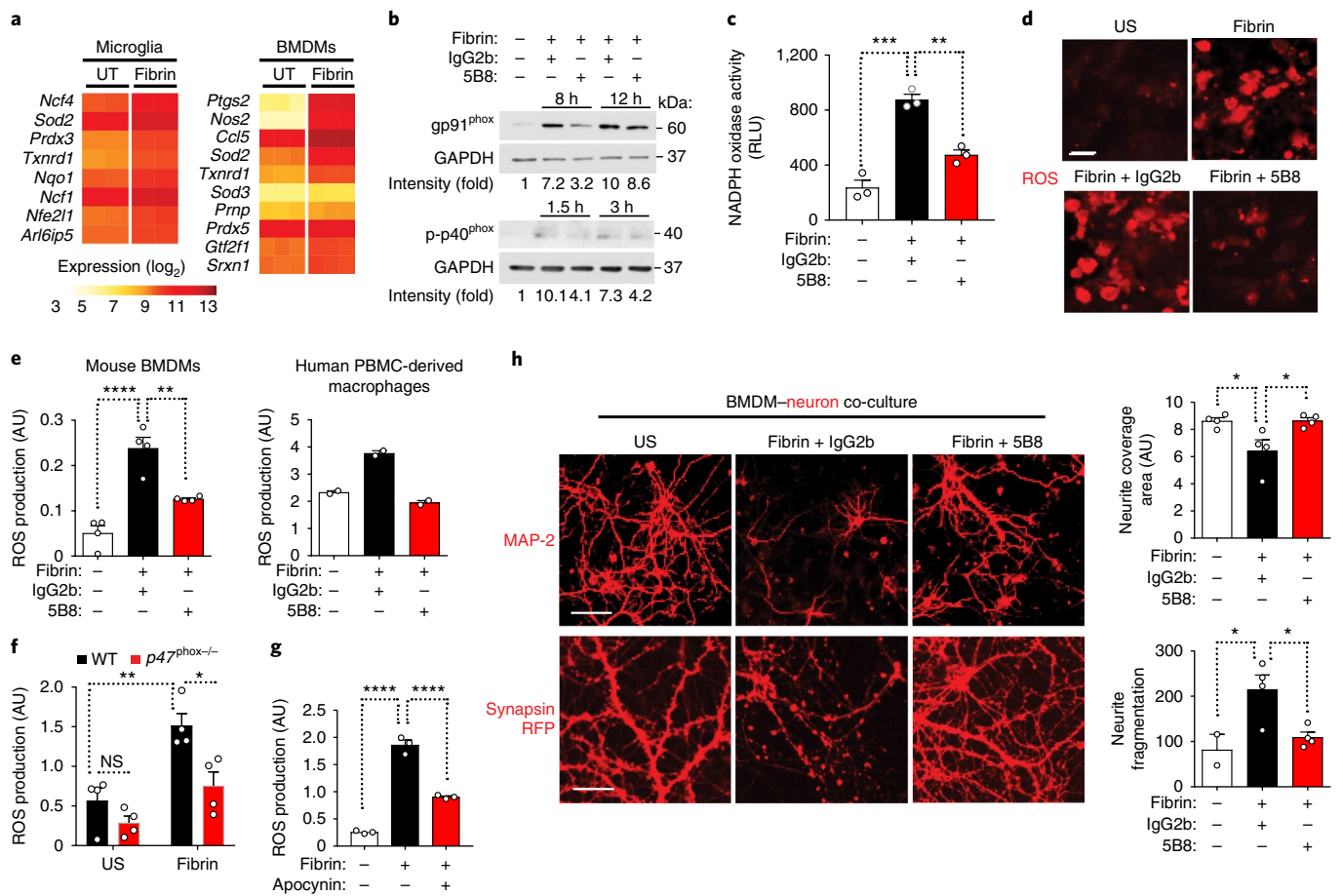


Fig. 3 | 5B8 blocks fibrin-induced ROS production and axonal damage. **a**, Expression (key below) of ROS-related genes (left margin) in microglia (left) and BMDMs (right) left untreated (UT) or treated with fibrin (above plots), showing genes with significantly differential expression in fibrin-treated cells relative to that in untreated cells ($|\log_2 \text{fold}| > 0.585$, and false-discovery rate < 0.05 (two-tailed moderated t -test)). Each column represents one sample from two independent experiments (microglia) or three independent experiments (BMDMs). **b**, Immunoblot analysis of gp91^{phox}, phosphorylated (p-) p40^{phox} and GAPDH (loading control) in BMDMs left untreated (far left lane) or stimulated for various times (above lanes) with fibrin in the presence of 5B8 or IgG2b (grid above blots); right margin, molecular size in kilodaltons (kDa); numbers below lanes indicate densitometry, presented as band intensity of gp91^{phox} (top) or phosphorylated p40^{phox} (bottom) relative to that of GAPDH (cropped blot images; full blots, Supplementary Fig. 9). Data are from one experiment representative of three independent experiments. **c**, NADPH oxidase activity in BMDMs left unstimulated or stimulated for 12 h with fibrin in the presence of 5B8 or IgG2b (grid below plot). Data are from three independent experiments (mean \pm s.e.m.). $**P = 0.0015$ and $***P = 0.0001$ (one-way ANOVA with Tukey's multiple-comparisons test). **d**, Microscopy of ROS production by BMDMs left unstimulated (US) or stimulated with fibrin alone or in the presence of 5B8 or IgG2b (above images), detected with dihydroethidium (DHE) (red). Scale bar, 10 μm . Data are representative of three independent experiments with similar results. **e**, Quantification of ROS production (assessed via DHE) in BMDMs (left) and human macrophages derived from peripheral blood mononuclear cells (PBMC) (right) left unstimulated or stimulated for 48 h with fibrin in the presence of 5B8 or IgG2b (grid below plot), presented in arbitrary units (AU). Data are from four (left) or two (right) independent experiments (mean \pm s.e.m.). $**P = 0.0033$ and $****P < 0.0001$ (one-way ANOVA with Bonferroni multiple-comparisons test). **f**, Quantification of ROS production in BMDMs isolated from wild-type mice (WT) and mice with genetic ablation of p47^{phox} (*Ncf1*^{-/-}; called 'p47^{phox}^{-/-}' here) (key) and left unstimulated (US) or stimulated for 24 h with fibrin (horizontal axis). Data are from $n = 4$ mice per group (mean \pm s.e.m.). $*P = 0.0204$ and $**P = 0.0040$ (two-way ANOVA with Sidak's multiple-comparisons test). **g**, Quantification of ROS production (assessed via DHE) in mouse BMDMs left unstimulated or stimulated for 24 h with fibrin in the presence or absence of apocynin (grid below plot). Data are from three independent experiments (mean \pm s.e.m.). $****P < 0.0001$ (one-way ANOVA with Tukey's multiple-comparisons test). **h**, Microscopy (left) of MAP-2 (top row) and synapsin-RFP (bottom row) in cortical neurons co-cultured with BMDMs left unstimulated (US) or stimulated with fibrin in the presence of 5B8 or IgG2b (above images); right, quantification of MAP-2⁺ neurite coverage (top) and neurite fragmentation assessed with synapsin-RFP (bottom) among co-cultures as at left (grid below plot). Scale bars (left), 50 μm (top) or 30 μm (bottom). Data are from four independent experiments (mean \pm s.e.m.). $*P = 0.0385$ (US vs fibrin + IgG2b; top), 0.0370 (fibrin + IgG2b vs fibrin + 5B8; top) or 0.0168 (fibrin + IgG2b versus fibrin + 5B8; bottom) (one-way ANOVA with Bonferroni multiple-comparisons test). Each symbol (**c**–**h**) represents an individual experiment (**c**,**e**,**g**,**h**) or mouse (**f**).

Given prophylactically, 5B8 reduced the mean maximum clinical score and delayed the first day of onset relative to those of groups treated with IgG2b (Supplementary Tables 1 and 2). Given therapeutically, 5B8 reduced the severity of relapses in PLP_{139–151} EAE (Fig. 4b and Supplementary Table 1). In all EAE treatment groups,

5B8 reduced the proportion of paralyzed mice (Fig. 4c). Fibrin is a cross-linked polymer of fibrinogen molecules. Consequently, antibodies to fibrinogen detect both fibrinogen and fibrin¹¹. Fibrinogen is converted to fibrin at sites of increased coagulation activity¹¹. In the spinal cord during EAE, coagulation activity promotes the

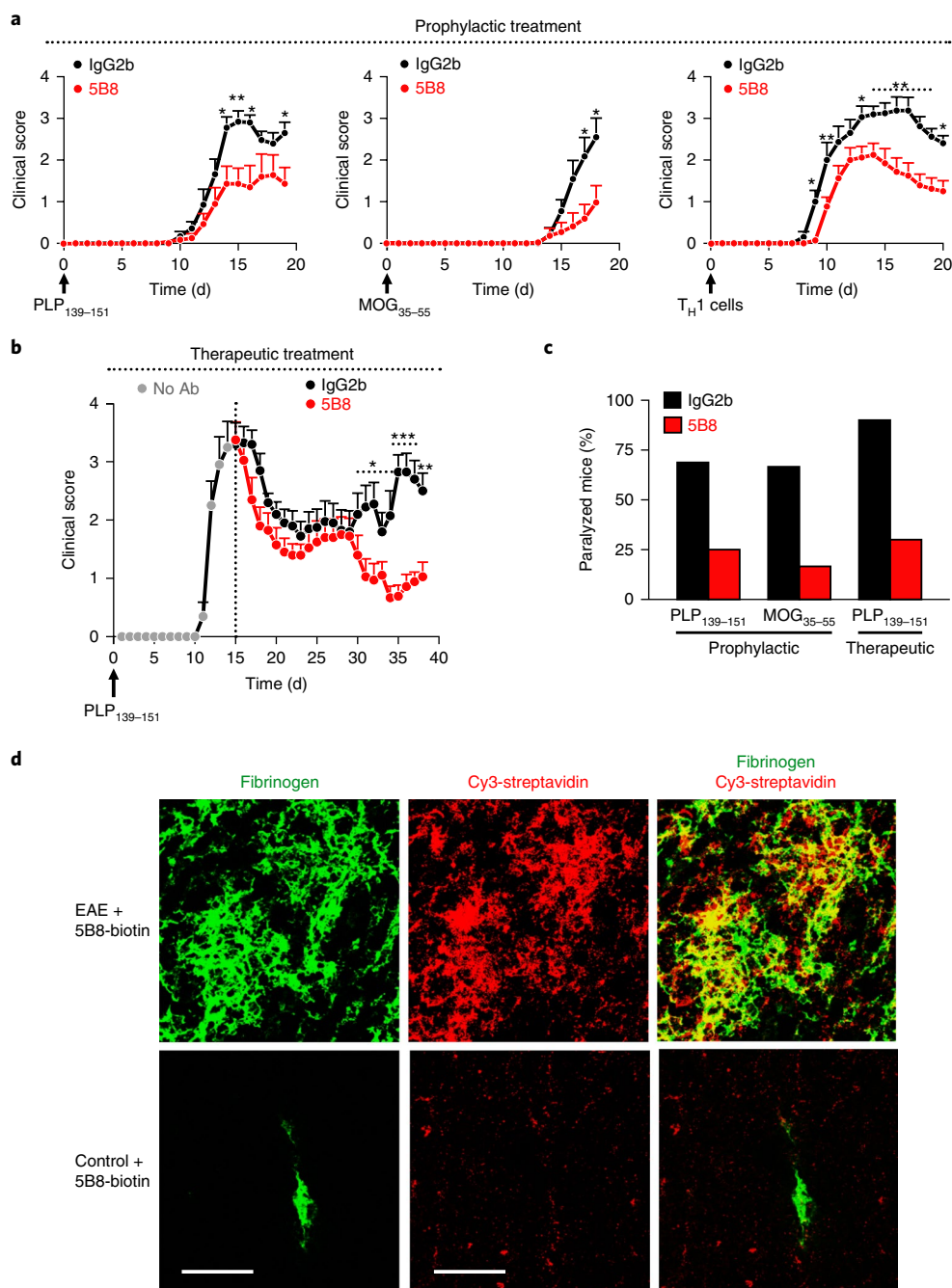


Fig. 4 | 5B8 suppresses EAE and engages fibrin target. **a**, Clinical scores for EAE of mice in which EAE was induced on day 0 (upward arrow) with PLP₁₃₉₋₁₅₁ (left), MOG₃₅₋₅₅ (middle) or adoptive transfer of T_H1 cells (right), followed by prophylactic administration of 5B8 (800 μg) or IgG2b (800 μg) (key) every 2 d from day 0. Data are from PLP₁₃₉₋₁₅₁ EAE, *n* = 16 mice (IgG2b), *n* = 16 mice (5B8); MOG₃₅₋₅₅ EAE, *n* = 11 mice (IgG2b), *n* = 12 mice (5B8); adoptive transfer T_H1 EAE, *n* = 15 mice (IgG2b) or *n* = 24 mice (5B8) (mean + s.e.m.). **P* < 0.05 and ***P* < 0.01 (linear mixed effects model with two-tailed permutation test). **b**, Clinical scores for PLP₁₃₉₋₁₅₁ EAE mice given no antibody injection or therapeutic injection of 5B8 or IgG2b (key) every 2 d starting at the peak of the initial paralytic episode (dotted vertical line). Data are from *n* = 10 mice (IgG2b) or *n* = 10 mice (5B8) (mean + s.e.m.). **P* < 0.05, ***P* < 0.01 and ****P* < 0.001 (linear mixed-effects model with two-tailed permutation test). **c**, Proportion of mice with partial or complete hindlimb paralysis (score > 2.5) among mice with PLP₁₃₉₋₁₅₁ or MOG₃₅₋₅₅ EAE (horizontal axis) given prophylactic or therapeutic treatment (below plots) with 5B8 or IgG2b (key). **d**, Confocal microscopy of spinal cord sections from mice with MOG₃₅₋₅₅ EAE (top row) and healthy non-immunized control mice (bottom) given intraperitoneal injection of biotinylated 5B8, showing the spatial correlation (yellow) between biotinylated 5B8, detected with Cy3-streptavidin (red), and fibrin deposition, detected with antibody to fibrin(ogen) (green). Scale bars, 200 μm. Data are representative of *n* = 3 mice per group.

conversion of fibrinogen to fibrin, which leads to parenchymal deposition of fibrin at areas of microglial activation and demyelination²⁷. After intraperitoneal injection of biotinylated 5B8 into mice with EAE, 5B8 spatially correlated with fibrin(ogen)-rich areas in the spinal cord (Fig. 4d), which demonstrated engagement of the target.

To determine whether 5B8 inhibited the recruitment of inflammatory cells into the CNS, we induced EAE in *Cx3cr1*^{GFP/+}*Ccr2*^{RFP/+} mice (in which chemokine receptor CX3CR1⁺ microglia express green fluorescent protein (GFP), and chemokine receptor CCR2⁺ macrophages express red fluorescent protein (RFP)) and then

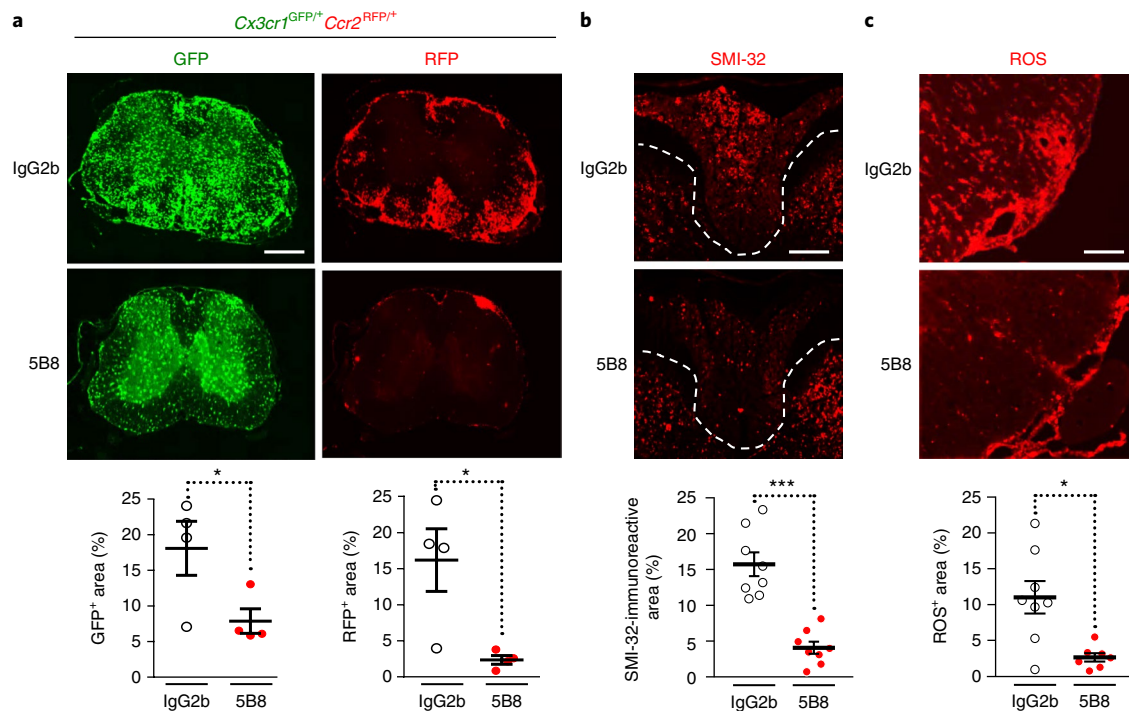


Fig. 5 | 5B8 inhibits microglial activation, monocyte recruitment and axonal damage in EAE. **a**, Microscopy (top group) of spinal cord sections from *Cx3cr1^{GFP/+}Ccr2^{RFP/+}* mice with MOG₃₅₋₅₅ EAE, treated with 5B8 or IgG2b (left margin), showing CX3CR1⁺ microglia (green) and CCR2⁺ macrophages (red); bottom, quantification of CX3CR1⁺ microglia (left) and CCR2⁺ macrophages (right) in spinal cords of mice as above (horizontal axis), 500 μ m. Data are from $n = 4$ mice per group. * $P = 0.0495$ (left) or 0.0286 (right) (two-tailed Mann-Whitney test). **b**, Microscopy (top) of spinal cords from mice with PLP₁₃₉₋₁₅₁ EAE, treated with 5B8 or IgG2b (left margin), showing SMI-32 immunoreactivity (indicative of axonal damage); dashed lines demarcate white matter of the spinal cord dorsal column. Bottom, quantification of results in mice as above (horizontal axis), presented as the proportion of the area with SMI-32 immunoreactivity. Scale bar (top), 200 μ m. Data are from $n = 8$ mice per group. *** $P = 0.0002$ (two-tailed Mann-Whitney test). **c**, Microscopy (top) of spinal cords from mice as in **b**, showing ROS detection. Quantification of ROS (assessed via DHE) in mice as above (horizontal axis). Scale bar (top), 100 μ m. Data are from $n = 8$ mice (IgG2b) or $n = 7$ mice (5B8). * $P = 0.0140$ (two-tailed Mann-Whitney test). Each symbol (bottom row) represents an individual mouse; small horizontal lines indicate the mean (\pm s.e.m.).

treated these mice with 5B8. We found that 5B8 inhibited both the accumulation of CX3CR1⁺ microglia and the infiltration of CCR2⁺ monocytes into the CNS in these mice (Fig. 5). Increased NADPH oxidase activity and excessive ROS production have been linked to MS²⁸, and ROS generated by invading and resident CNS macrophages mediate demyelination and axonal damage in EAE⁷. 5B8 markedly diminished axonal damage, the generation of ROS, inflammation and demyelination in EAE (Fig. 5 and Supplementary Fig. 5a,b). In accordance with published studies^{7,12}, axonal damage correlated with ROS⁺ areas in EAE lesions (Supplementary Fig. 5c). The fibrin peptide $\gamma_{377-395}$ inhibits the binding of fibrin to CD11b and suppresses EAE without affecting peripheral T cell responses¹³. Similarly, 5B8 did not significantly alter peripheral T cell responses in mice with PLP₁₃₉₋₁₅₁ EAE (CD4⁺ T cells, $P = 0.8413$; CD8⁺ T cells, $P = 0.4048$ (two-tailed Mann-Whitney test); Supplementary Fig. 6), which suggested that 5B8 did not modulate peripheral adaptive immune responses. These results suggested that systemic delivery of 5B8 in vivo was well tolerated and that fibrin-targeting immunotherapy suppressed the activation of innate immunity, oxidative stress, demyelination and axonal damage in EAE.

Fibrin-targeting immunotherapy protects mice with AD. Neurodegeneration driven by the innate immune system has emerged as a key pathogenic mechanism in AD⁵. We therefore investigated whether blocking fibrin–CD11b interactions protected mice against amyloid-related neurodegeneration. In 5XFAD mice (in which transgenes encoding familial AD mutant forms of human

amyloid precursor protein and presenilin 1 are expressed in neurons), fibrin was detected in the brain as early as 3 months of age; at 5 months, fibrin accumulation was abundant at sites of amyloid- β (A β) deposition, which were surrounded by CD11b⁺ microglia (Fig. 6a and Supplementary Fig. 7a). Also in accordance with prior findings in TgCRND8 mice (which overexpress human amyloid precursor protein)²⁹, fibrin deposits were detected in 5XFAD mice in the vicinity of dystrophic neurites (Fig. 6b), a key feature of neurodegeneration in AD³⁰. Systemically administered 5B8 spatially correlated with fibrin-rich areas surrounding A β plaques in 5XFAD mice (Fig. 6c and Supplementary Fig. 7b), which demonstrated penetration of the brain and engagement of the target.

To determine whether blocking fibrin–CD11b interactions protected mice against amyloid-related neurodegeneration, we treated 5XFAD mice with 5B8 for 2 months, starting at 3.5 months of age (1.5 months after the appearance of A β plaques and microglial activation) (Fig. 7a). Treatment with 5B8 reduced the loss of cholinergic neurons and microglial activation around plaques in 5XFAD mice (Fig. 7b,c) without significantly affecting A β plaques or the number of MAC-2⁺ macrophages around plaques ($P = 0.1142$ (two-tailed Mann-Whitney test); Supplementary Fig. 8a,b). Whole-genome microarray and GO analysis of cortical gene expression in 5XFAD mice showed that 5B8 suppressed five key pathways: the complement pathway, antigen presentation, cytokine response, lysozyme and ROS (Fig. 7d). Overall, these findings suggested that blocking fibrin–CD11b signaling suppressed amyloid-induced neurodegeneration and reduced the expression of genes encoding molecules that promote inflammation and oxidative stress.

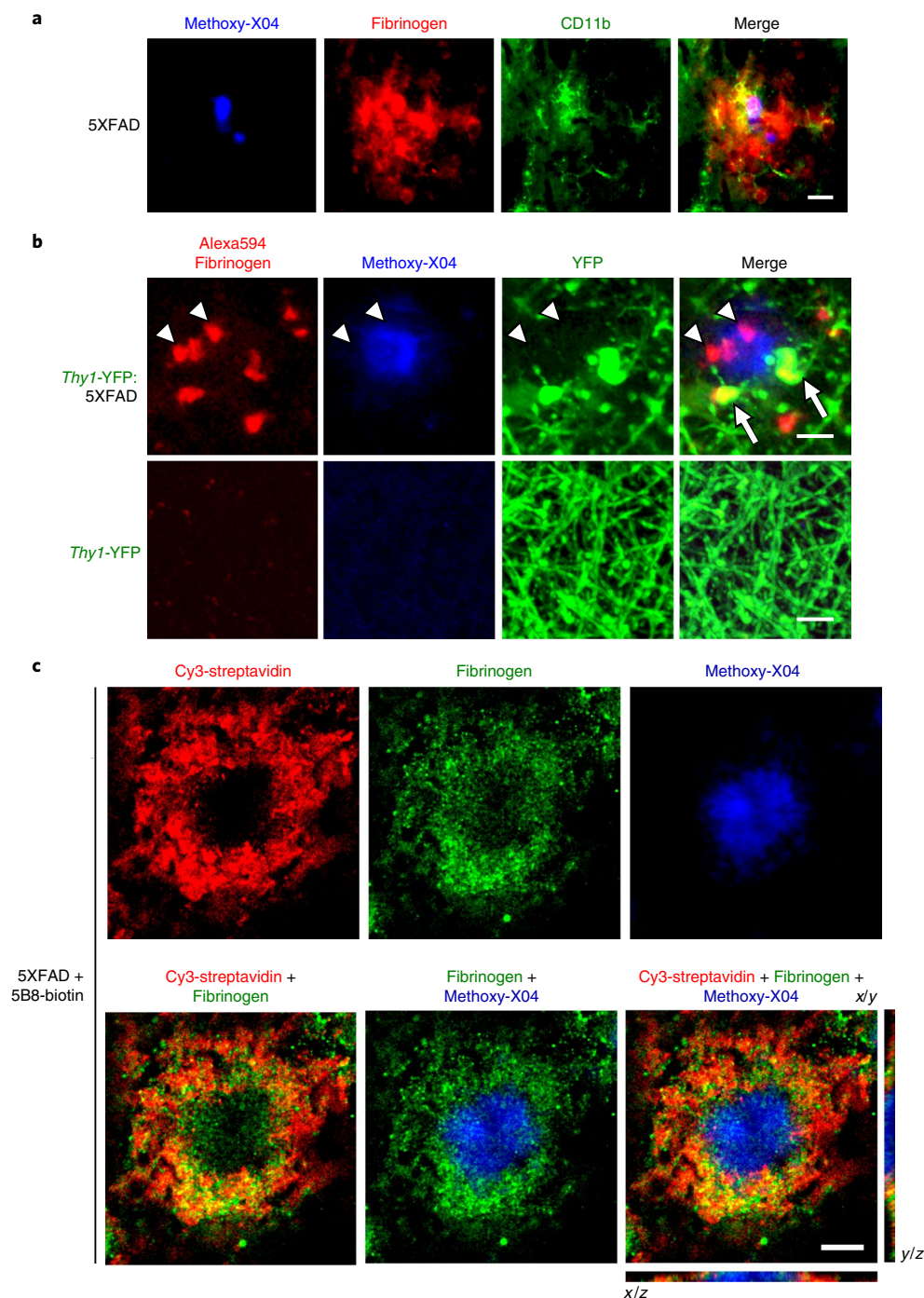


Fig. 6 | 5B8 target engagement in 5XFAD mice. **a**, Microscopy of a cortical section from a 3-month-old 5XFAD mouse co-labeled for fibrinogen (red), CD11b (green), and an A β plaque (blue). Scale bar, 20 μ m. Data are representative of $n = 4$ mice. **b**, In vivo two-photon imaging of cortex from an 11-month-old *Thy1*-YFP mice (expressing yellow fluorescent protein (YFP) in neurons) and an age-matched *Thy1*-YFP:5XFAD mouse (left margin) given intravenous injection of Alexa Fluor 594-conjugated fibrinogen (red), Methoxy-X04+ A β plaque (blue), and dystrophic neurites (green, swollen green structures); arrowheads indicate fibrinogen (red) surrounding an A β plaque (blue) at areas of neuritic loss; arrows indicate fibrinogen extravasation at areas of dystrophic neurites (yellow) in close proximity to a plaque (blue). Scale bars, 10 μ m. Data are representative of $n = 4$ mice (*Thy1*-YFP:5XFAD) or $n = 2$ mice (*Thy1*-YFP). **c**, Microscopy of brain sections from an 5XFAD mouse given intraperitoneal injection of biotinylated 5B8, stained with Cy3-streptavidin (red) and antibody to fibrinogen (green), showing a Methoxy-X04+ A β plaque (blue); bottom right, orthogonal views of the y/z and x/z planes show the localization of fibrinogen and 5B8 around amyloid plaques. Scale bar, 10 μ m. Data are representative of $n = 3$ mice.

Fibrin-targeting immunotherapy suppresses genes of the *TYROBP* network. Gene-network analysis has broadened the understanding of AD pathogenesis by revealing immunological gene networks as probable causal contributors to AD pathology³¹.

Targeting these networks could culminate in the development of novel therapeutics. To identify gene networks that might be regulated by 5B8, we investigated our transcriptomics data by biological network analysis. First, we performed genetic network modeling

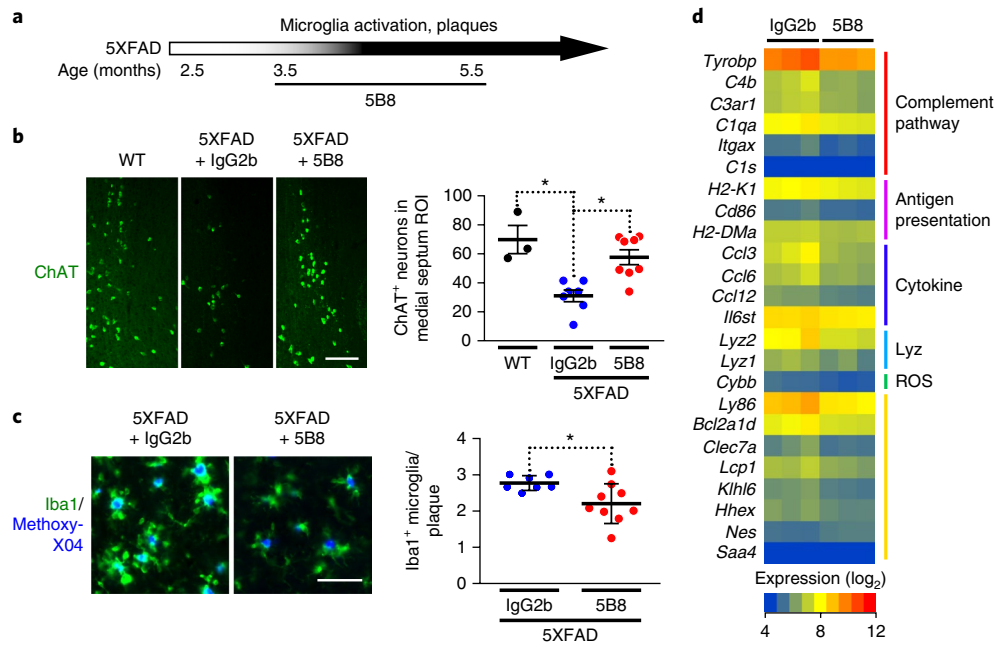


Fig. 7 | 5B8 protects 5XFAD mice against neurodegeneration and inflammatory responses. **a**, Protocol for the administration of 5B8 or IgG2b isotype control to 5XFAD mice: 800 μ g injected intraperitoneally every other day for 2 months starting at 3.5 months of age, after the appearance of plaques and microglial activation. **b**, Microscopy (left) of the medial septum of 5XFAD mice treated with IgG2b or 5B8 (above images) and their untreated, non-transgenic littermates (WT), showing ChAT⁺ cholinergic neurons; right, quantification of ChAT⁺ neurons in each region of interest (ROI) in mice as at left (horizontal axis). Scale bar (left), 80 μ m. Each symbol (right) represents an individual mouse; small horizontal lines indicate the mean (\pm s.e.m.). Data are from $n=3$ mice (WT), $n=7$ mice (5XFAD + IgG2b) or $n=8$ (5XFAD + 5B8). * $P=0.0211$ (WT vs IgG2b) or 0.0157 (IgG2b vs 5B8) (Kruskal-Wallis with Dunn's multiple-comparisons test). **c**, Microscopy (left) of the cortex of 5XFAD mice treated with IgG2b or 5B8 (above images), showing Iba-1⁺ cells (green) around Methoxy-X04⁺ plaques (blue); right, quantification of plaque-associated Iba-1⁺ microglia. Scale bar (left), 50 μ m. Each symbol (right) represents an individual mouse; small horizontal lines indicate the mean (\pm s.e.m.). Data are from $n=7$ mice (IgG2b) or $n=9$ mice (5B8). * $P=0.0337$ (two-tailed Mann-Whitney test). **d**, Affymetrix microarray analysis of the expression (key) of genes (left margin) (right margin; labeling of immune functions identified after GO-Elite analysis) in the cortex of 5XFAD mice treated with 5B8 or IgG2b (above plots). $P < 0.05$ (two-tailed, raw; moderated t -test).

of genes downregulated by 5B8. Co-expression analysis revealed 5B8-downregulated genes to be densely interconnected encoding molecules mainly of the complement pathway, including *C4b* and *C1q*, with *Tyrobp* (which encodes the adaptor DAP12) forming a major hub (Fig. 8a). The cluster of co-expressed genes downregulated by 5B8 showed a striking overlap with networks of genes encoding molecules linked to the pathogenesis of human AD, including those encoding the TYROBP-related microglial module³¹. Indeed, *Tyrobp*, which encodes a co-receptor for CD11b and the human AD-associated receptor Trem2, was one of the genes with the greatest degree of downregulation by 5B8 (Figs. 7d and 8a). Overlay of gene-expression data obtained from 5B8-treated 5XFAD mice with networks of genes encoding neuroinflammatory molecules from brains of humans with AD showed a reduction in the expression of genes in the human AD-related inflammatory networks by 5B8. By overlaying our data onto a mouse version of the human AD TYROBP module³¹, we found that 5B8 downregulated 65% of the *Tyrobp*-related network at various levels of significance, including *Tyrobp* at the nexus of the network (Fig. 8b). Several components of the TYROBP signaling pathway were also downregulated (Supplementary Fig. 8c). This bioinformatics approach allowed us to gain insight into the mechanisms of action of treatment with 5B8, as we identified downregulation mainly of co-expressed genes encoding components of the complement pathway that were relevant to the pathogenesis of AD. Integrated gene network analysis might be a useful tool with which to better understand the mechanism of action of new drugs and assess their efficacy in suppressing inflammatory gene networks relevant to human disease. Thus, the inhibition of fibrin by 5B8 might suppress the pathogenic activation

of innate immunological pathways that mediate amyloid-related neurodegeneration.

Discussion

Our study has revealed a previously unknown neurodegenerative pathway in which fibrin activated NADPH oxidase in innate immune cells to promote ROS production and neurotoxicity. By developing an antibody-based approach to selectively target a key inflammatory fibrin domain, we showed here that fibrin-targeting immunotherapy can be selective and efficacious in suppressing neuroinflammation and neurodegeneration. Consequently, preventing fibrin from engaging this mechanism might lead to the development of therapeutic strategies for the treatment of neurodegenerative diseases with neurovascular dysfunction. This discovery might have implications beyond the CNS, since fibrin deposition is a common thread in inflammatory pathologies, such as rheumatoid arthritis, colitis and Duchenne muscular dystrophy (reviewed in refs ^{11,12}). Fibrin-CD11b signaling induces chemokine release and macrophage recruitment¹⁶ and increased activation of NADPH oxidase, which culminates in the release of ROS and oxidative stress (as we have shown here). Therefore, inhibitors of the fibrin-CD11b interaction, such as 5B8, have the potential to affect both inflammatory processes and oxidative stress. Inhibiting the formation of fibrin with anticoagulants can cause adverse effects by increasing the risk of bleeding³². Epitope-selective targeting of fibrin might overcome that challenge through selective suppression of its damaging functions without adverse anticoagulant effects. Overall, fibrin-targeting immunotherapy might represent a selective multi-indication therapy for the suppression of fibrin-induced chronic inflammation

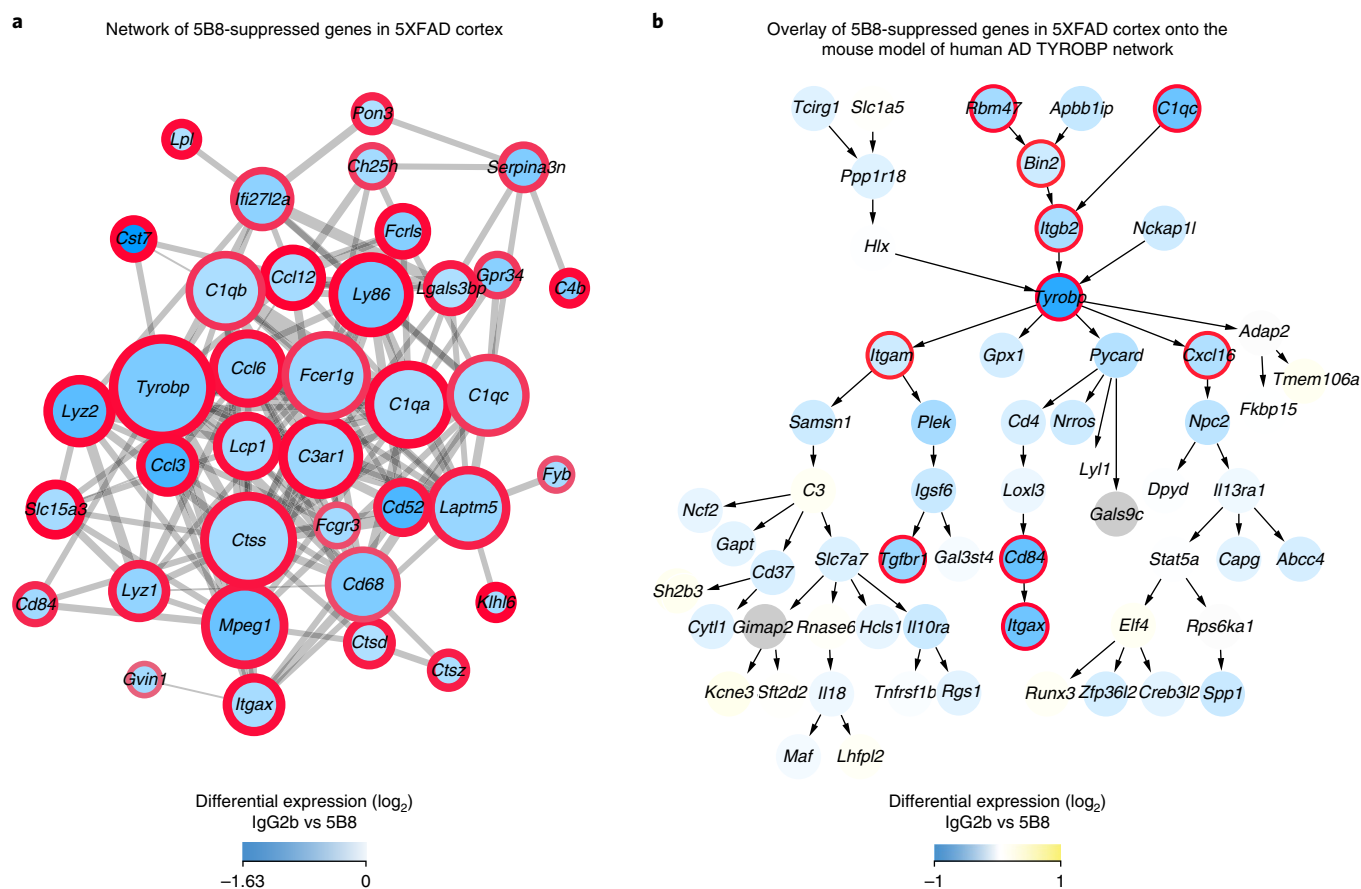


Fig. 8 | 5B8 suppresses the complement-TYROBP microglial module in 5XFAD mice. **a**, Co-expression analysis of genes downregulated by 5B8 (selected from those with change in expression of -0.5 -fold or less (\log_2 values) and a raw P value of <0.05 (two-tailed moderated t -test)): intensity of blue shading (key) indicates the extent of the decrease in expression after 5B8 treatment relative to expression after IgG2b treatment; thickness of the red border indicates the significance of the difference in expression; circle size indicates the number of connected genes in the network. **b**, Mouse model of the human AD TYROBP network with data overlay of the genes downregulated by 5B8 in 5XFAD mice: yellow-blue gradient of shading (key) indicates differential expression; thickness of the red border indicates significance of $P < 0.05$ (two-tailed moderated t -test).

through inhibition of the release of proinflammatory factors and oxidative stress at sites of increased vascular permeability in neurological and other inflammatory diseases.

Our study has revealed a previously unknown function for fibrin-CD11b signaling as an activator of NADPH oxidase-dependent production of ROS. CD11b-dependent respiratory bursts require signaling via DAP12³³. CD11b and DAP12 are co-expressed in microglia and act synergistically to promote the production of superoxide ions and induce neuronal death³³. Intriguingly, DAP12 was a major pathway downregulated by fibrin-targeting immunotherapy in the 5XFAD mouse brain. Fibrin (via activation of CD11b-CD18 signaling) might increase DAP12 expression and potentiate oxidative damage dependent on CD11b-DAP12 by promoting phosphorylation and assembly of the NADPH oxidase complex^{34,35} and activating kinase pathways¹³. In addition to fibrin, several other immunologically mediated mechanisms can activate NADPH oxidase, such as the binding of A β to the scavenger receptor CD36 or the activation of CD11b-CD18 or receptor TLR4 signaling by α -synuclein or LPS²⁵. A β -induced activation of NADPH oxidase in innate immune cells contributes to neurovascular dysfunction, neurodegeneration and cognitive decline in mice with AD^{5,36}. Fibrin and A β might have an additive effect on the activation of NADPH oxidase via CD11b-CD18 and CD36, respectively. Genome-wide association studies, converged linkage analysis and gene-expression data have indicated immunological regulation of AD pathology. Such studies, in combination with the limited success of clinical

trials in which amyloid is targeted, have led to a reassessment of the pathogenesis of AD and the need for the development of new treatments directed against different targets³⁷. Vascular pathologies and amyloid pathologies are independent and additive predictors of cognitive decline in the elderly^{38,39}, which suggests that they might need to be targeted independently for maximal therapeutic benefit. Fibrin-targeting immunotherapy did not reduce the deposition of A β after 2 months of administration, which would suggest that its neuroprotective effects occur in the presence of A β . Future studies should determine whether 5B8 also affects cognitive performance in mice with AD.

Fibrin-targeting immunotherapy represents a novel approach with which to selectively suppress pathogenic innate immune responses with potential clinical implications. In MS, anti-inflammatory medications have little effect during the progressive phase of disease, which is mediated by innate immunological mechanisms^{3,8}. Other modulators of innate immunity, such as complement, CR3, TNF, NF- κ B, PI3K and TLR4, are ubiquitously expressed in the brain and the periphery and have reported roles in regulating physiological CNS functions. In contrast, fibrin is not present in the normal brain but is abundantly deposited in the CNS after disruption of the BBB¹¹. 5B8 was selective in inhibiting the activation of innate immunity via targeting fibrin and did not affect the activation of macrophages by other ligands, such as LPS, which suggested that the activation of innate immunity by other ligand-receptor interactions could proceed normally. Phagocytic pathways in innate

immune cells are required for the clearance of debris and remyelination⁴⁰. Fibrin-primed macrophages inhibit the differentiation of oligodendrocyte precursor cells⁴¹, which are susceptible to oxidative stress⁴². Fibrin-targeting immunotherapy could suppress fibrin-induced chronic inflammation and potentially promote repair by inhibiting oxidative stress and the release of proinflammatory factors. Microglia and macrophages are functionally distinct populations with diverse functions in neurodegenerative diseases^{43–46}. Studies using mass cytometry and large transcriptomics profiling of microglia and macrophages will be needed to determine the potential differential effects of fibrin on innate immune cell populations. The inflammatory epitope $\gamma_{377-395}$ of fibrin has been confirmed genetically in inflammatory models in the brain and periphery with findings replicated in numerous laboratories (reviewed in refs^{11,12}). It is possible that pharmacological targeting of fibrin might represent a selective treatment to add to the toolbox of therapies directed against innate immunity that might be particularly efficacious for suppressing neuroinflammation at sites of BBB leakage and vascular damage with fibrin deposition.

The genetic and pharmacological tools available for studying the epitope $\gamma_{377-395}$ (*Fgg*^{390–396A} mice, which express a $\gamma_{390-396A}$ mutant fibrinogen γ -chain; the $\gamma_{377-395}$ peptide; and antibody 5B8 in our study here) have revealed mainly pathogenic functions for the epitope $\gamma_{377-395}$ in inflammation. *Fga*^{-/-} mice, which lack fibrinogen, and *Fgg*^{390–396A} mice^{13,47,48}, as well as mice treated with 5B8 (as in our study here), with $\gamma_{377-395}$ peptide¹³ or with anticoagulants^{13,26,41}, are not immunocompromised and can be housed in conventional animal facilities without opportunistic infections. In humans, congenital afibrinogenemia, a genetic disorder characterized by a complete absence of fibrinogen, is associated with excessive bleeding but no increase in opportunistic infections⁴⁹. Fibrin inhibits repair, as persistent deposition of fibrin inhibits wound healing⁵⁰, while depletion of fibrin increases remyelination^{41,51}. Such studies do not exclude the possibility that the fibrinogen epitope $\gamma_{377-395}$ might have physiological functions that have not yet become apparent through the use of the genetic and pharmacologic tools available. Collectively, prior genetic studies of the $\gamma_{377-395}$ epitope and our findings here support the proposal that fibrin induces, in a ligand-selective manner, a specific gene signature in immune cells that produces mainly pathogenic functions. Consequently, targeting fibrin-induced activation of innate immunity has the potential to suppress proinflammatory and neurotoxic pathways without substantial interference with protective functions of the innate immune system. Immunotoxicology studies will also be needed in the future to fully test potential immunological dysfunction in the context of fibrin-targeting immunotherapy.

Fibrinogen is a coagulation factor essential for blood clotting. Studies of *Fgg*^{390–396A} mice have shown that the epitope $\gamma_{377-395}$ is not required for fibrin polymerization or platelet aggregation and does not increase bleeding risk⁴⁸. *Fgg*^{390–396A} mice have normal concentrations of fibrinogen, fibrin polymerization and platelet aggregation, normal thrombus formation in FeCl₃-injured carotid arteries, and normal pregnancy and birth rates. Furthermore, they do not develop spontaneous hemorrhagic events and tolerate major surgical procedures (such as abdominal surgeries) without inordinate bleeding⁴⁸. In contrast to *Fgg*^{390–396A} mice, *Fga*^{-/-} mice, which lack fibrinogen exhibit broad hemostatic abnormalities secondary to the lack of clotting function and failure of fibrinogen-supported platelet aggregation and uniformly cannot sustain pregnancy due to the hemostatic requirements at the placental–maternal interface⁴⁷, a phenotype also observed in mice that lack the transglutaminase fXIII⁵². Consistent with experimental findings for *Fgg*^{390–396A} mice, the fibrin peptide $\gamma_{377-395}$ does not inhibit normal clotting time in vivo or fibrin polymerization in vitro¹³. Our study has shown that 5B8 did not affect normal clotting time in vivo, fibrin polymerization in vitro or aPTT in human plasma. Similar to *Fgg*^{390–396A}

mice, mice treated with 5B8 even for prolonged periods of up to ~2 months did not develop any spontaneous bleeding. The $\gamma_{377-395}$ epitope targeted by 5B8 does not overlap with the $\gamma_{398-406}$ residues known to be enzymatically cross-linked by fXIII⁵³. Nevertheless, comparative studies of fXIII-mediated crosslinking in vitro and in vivo will be of interest in future studies of 5B8. This could be of particular interest in light of studies of *Fgg*^{390–396A} mice in a model of venous thrombosis⁵⁴. In those studies, *Fgg*^{390–396A} mice were shown to maintain fXIII-mediated cross-linking of the γ -chain but at a reduced rate, and this resulted in smaller venous thrombi. Overall, studies of *Fgg*^{390–396A} mice⁴⁸, data obtained with the fibrin peptide $\gamma_{377-395}$ (ref. 13) and our results in this study suggest that the epitope $\gamma_{377-395}$ and 5B8 do not interfere with fibrin clotting and present a limited risk of spontaneous hemorrhagic events. Additional toxicology studies will be needed to determine whether 5B8 interferes with other features of hemostasis and thrombosis.

Together, data from human pathology, genetic and pharmacological studies of mice, transcriptomics and signal-transduction studies have established fibrin as a dual inflammatory and oxidative-stress signal in the CNS and suggest that fibrin-targeting immunotherapy might prevent neurodegeneration and other complications in conditions associated with fibrin deposits at sites of disruption of the BBB. Fibrin-targeting immunotherapy might hold promise as a new therapeutic strategy for neurological and inflammatory disorders with vascular damage.

Online content

Methods, including statements of data availability and any associated accession codes and references, are available at <https://doi.org/10.1038/s41590-018-0232-x>.

Received: 17 June 2017; Accepted: 7 September 2018;

Published online: 15 October 2018

References

- Rivest, S. Regulation of innate immune responses in the brain. *Nat. Rev. Immunol.* **9**, 429–439 (2009).
- Ransohoff, R. M. & Brown, M. A. Innate immunity in the central nervous system. *J. Clin. Invest.* **122**, 1164–1171 (2012).
- Lassmann, H., van Horssen, J. & Mahad, D. Progressive multiple sclerosis: pathology and pathogenesis. *Nat. Rev. Neurol.* **8**, 647–656 (2012).
- Schuh, C. et al. Oxidative tissue injury in multiple sclerosis is only partly reflected in experimental disease models. *Acta Neuropathol.* **128**, 247–266 (2014).
- Heppner, F. L., Ransohoff, R. M. & Becher, B. Immune attack: the role of inflammation in Alzheimer disease. *Nat. Rev. Neurosci.* **16**, 358–372 (2015).
- Lassmann, H. Mechanisms of neurodegeneration shared between multiple sclerosis and Alzheimer's disease. *J. Neural Transm. (Vienna)* **118**, 747–752 (2011).
- Nikić, I. et al. A reversible form of axon damage in experimental autoimmune encephalomyelitis and multiple sclerosis. *Nat. Med.* **17**, 495–499 (2011).
- Chitnis, T. & Weiner, H. L. CNS inflammation and neurodegeneration. *J. Clin. Invest.* **127**, 3577–3587 (2017).
- Frischer, J. M. et al. The relation between inflammation and neurodegeneration in multiple sclerosis brains. *Brain* **132**, 1175–1189 (2009).
- Zhao, Z., Nelson, A. R., Betsholtz, C. & Zlokovic, B. V. Establishment and dysfunction of the blood–brain barrier. *Cell* **163**, 1064–1078 (2015).
- Petersen, M. A., Ryu, J. K. & Akassoglou, K. Fibrinogen in neurological diseases: mechanisms, imaging and therapeutics. *Nat. Rev. Neurosci.* **19**, 283–301 (2018).
- Davalos, D. & Akassoglou, K. Fibrinogen as a key regulator of inflammation in disease. *Semin. Immunopathol.* **34**, 43–62 (2012).
- Adams, R. A. et al. The fibrin-derived $\gamma_{377-395}$ peptide inhibits microglia activation and suppresses relapsing paralysis in central nervous system autoimmune disease. *J. Exp. Med.* **204**, 571–582 (2007).
- Ugarova, T. P. et al. Sequence $\gamma_{377-395}$ (P2), but not $\gamma_{190-202}$ (P1), is the binding site for the alpha MI-domain of integrin $\alpha_{M}\beta_2$ in the γ C-domain of fibrinogen. *Biochemistry* **42**, 9365–9373 (2003).
- Davalos, D. et al. Fibrinogen-induced perivascular microglial clustering is required for the development of axonal damage in neuroinflammation. *Nat. Commun.* **3**, 1227 (2012).
- Ryu, J. K. et al. Blood coagulation protein fibrinogen promotes autoimmunity and demyelination via chemokine release and antigen presentation. *Nat. Commun.* **6**, 8164 (2015).

17. Yates, R. L. et al. Fibrin(ogen) and neurodegeneration in the progressive multiple sclerosis cortex. *Ann. Neurol.* **82**, 259–270 (2017).
18. Marik, C., Felts, P. A., Bauer, J., Lassmann, H. & Smith, K. J. Lesion genesis in a subset of patients with multiple sclerosis: a role for innate immunity? *Brain* **130**, 2800–2815 (2007).
19. Lee, N. J. et al. Spatiotemporal distribution of fibrinogen in marmoset and human inflammatory demyelination. *Brain* **141**, 1637–1649 (2018).
20. Strickland, S. Blood will out: vascular contributions to Alzheimer's disease. *J. Clin. Invest.* **128**, 556–563 (2018).
21. Nathan, C. & Cunningham-Bussell, A. Beyond oxidative stress: an immunologist's guide to reactive oxygen species. *Nat. Rev. Immunol.* **13**, 349–361 (2013).
22. Fischer, M. T. et al. NADPH oxidase expression in active multiple sclerosis lesions in relation to oxidative tissue damage and mitochondrial injury. *Brain* **135**, 886–899 (2012).
23. Shimohama, S. et al. Activation of NADPH oxidase in Alzheimer's disease brains. *Biochem. Biophys. Res. Commun.* **273**, 5–9 (2000).
24. Ma, M. W. et al. NADPH oxidase in brain injury and neurodegenerative disorders. *Mol. Neurodegener.* **12**, 7 (2017).
25. Haslund-Vinding, J., McBean, G., Jaquet, V. & Vilhardt, F. NADPH oxidases in oxidant production by microglia: activating receptors, pharmacology and association with disease. *Br. J. Pharmacol.* **174**, 1733–1749 (2017).
26. Han, M. H. et al. Proteomic analysis of active multiple sclerosis lesions reveals therapeutic targets. *Nature* **451**, 1076–1081 (2008).
27. Davalos, D. et al. Early detection of thrombin activity in neuroinflammatory disease. *Ann. Neurol.* **75**, 303–308 (2014).
28. Haider, L. et al. Oxidative damage in multiple sclerosis lesions. *Brain* **134**, 1914–1924 (2011).
29. Cortes-Canteli, M., Mattei, L., Richards, A.T., Norris, E.H. & Strickland, S. Fibrin deposited in the Alzheimer's disease brain promotes neuronal degeneration. *Neurobiol. Aging*, **36**, 608–617 (2015).
30. DeKosky, S. T. & Scheff, S. W. Synapse loss in frontal cortex biopsies in Alzheimer's disease: correlation with cognitive severity. *Ann. Neurol.* **27**, 457–464 (1990).
31. Zhang, B. et al. Integrated systems approach identifies genetic nodes and networks in late-onset Alzheimer's disease. *Cell* **153**, 707–720 (2013).
32. Shoeb, M. & Fang, M. C. Assessing bleeding risk in patients taking anticoagulants. *J. Thromb. Thrombolysis* **35**, 312–319 (2013).
33. Mócsai, A. et al. Integrin signaling in neutrophils and macrophages uses adaptors containing immunoreceptor tyrosine-based activation motifs. *Nat. Immunol.* **7**, 1326–1333 (2006).
34. Bedard, K. & Krause, K. H. The NOX family of ROS-generating NADPH oxidases: physiology and pathophysiology. *Physiol. Rev.* **87**, 245–313 (2007).
35. Turnbull, I. R. & Colonna, M. Activating and inhibitory functions of DAP12. *Nat. Rev. Immunol.* **7**, 155–161 (2007).
36. Park, L. et al. Scavenger receptor CD36 is essential for the cerebrovascular oxidative stress and neurovascular dysfunction induced by amyloid- β . *Proc. Natl. Acad. Sci. USA* **108**, 5063–5068 (2011).
37. Cummings, J. Lessons learned from Alzheimer disease: clinical trials with negative outcomes. *Clin. Transl. Sci.* **11**, 147–152 (2018).
38. Vemuri, P. et al. Vascular and amyloid pathologies are independent predictors of cognitive decline in normal elderly. *Brain* **138**, 761–771 (2015).
39. Rabin, J. S. et al. Interactive associations of vascular risk and β -amyloid burden with cognitive decline in clinically normal elderly individuals: findings from the Harvard aging brain study. *JAMA Neurol.* **75**, 1124–1131 (2018).
40. Miron, V. E. et al. M2 microglia and macrophages drive oligodendrocyte differentiation during CNS myelination. *Nat. Neurosci.* **16**, 1211–1218 (2013).
41. Petersen, M. A. et al. Fibrinogen activates BMP Signaling in oligodendrocyte progenitor cells and inhibits remyelination after vascular damage. *Neuron* **96**, 1003–1012 (2017).
42. Oka, A., Belliveau, M. J., Rosenberg, P. A. & Volpe, J. J. Vulnerability of oligodendroglia to glutamate: pharmacology, mechanisms, and prevention. *J. Neurosci.* **13**, 1441–1453 (1993).
43. Butovsky, O. et al. Identification of a unique TGF- β -dependent molecular and functional signature in microglia. *Nat. Neurosci.* **17**, 131–143 (2014).
44. Ajami, B. et al. Single-cell mass cytometry reveals distinct populations of brain myeloid cells in mouse neuroinflammation and neurodegeneration models. *Nat. Neurosci.* **21**, 541–551 (2018).
45. Keren-Shaul, H. et al. A unique microglia type associated with restricting development of Alzheimer's disease. *Cell* **169**, 1276–1290.e17 (2017).
46. Mrdjen, D. et al. High-dimensional single-cell mapping of central nervous system immune cells reveals distinct myeloid subsets in health, aging, and disease. *Immunity* **48**, 380–395 (2018).
47. Suh, T. T. et al. Resolution of spontaneous bleeding events but failure of pregnancy in fibrinogen-deficient mice. *Genes Dev.* **9**, 2020–2033 (1995).
48. Flick, M. J. et al. Leukocyte engagement of fibrin(ogen) via the integrin receptor α M β 2/Mac-1 is critical for host inflammatory response in vivo. *J. Clin. Invest.* **113**, 1596–1606 (2004).
49. Lak, M., Keihani, M., Elahi, F., Peyvandi, F. & Mannucci, P. M. Bleeding and thrombosis in 55 patients with inherited afibrinogenemia. *Br. J. Haematol.* **107**, 204–206 (1999).
50. Bugge, T. H. et al. Loss of fibrinogen rescues mice from the pleiotropic effects of plasminogen deficiency. *Cell* **87**, 709–719 (1996).
51. Akassoglou, K., Yu, W.-M., Akpınar, P. & Strickland, S. Fibrin inhibits peripheral nerve remyelination by regulating Schwann cell differentiation. *Neuron* **33**, 861–875 (2002).
52. Koseki-Kuno, S., Yamakawa, M., Dickneite, G. & Ichinose, A. Factor XIII A subunit-deficient mice developed severe uterine bleeding events and subsequent spontaneous miscarriages. *Blood* **102**, 4410–4412 (2003).
53. Chen, R. & Doolittle, R. F. γ - γ cross-linking sites in human and bovine fibrin. *Biochemistry* **10**, 4487–4491 (1971).
54. Aleman, M. M. et al. Factor XIII activity mediates red blood cell retention in venous thrombi. *J. Clin. Invest.* **124**, 3590–3600 (2014).

Acknowledgements

We thank I.F. Charo (Gladstone Institutes) for *Ccr2*^{2RFP/RFP} mice on a C57BL/6 background; J.L. Degen for advice and critical reading of the manuscript; S. Pintchovski, I. Kadiu, J. Palop and J. Egebjerg for discussions; B. Cabriga, R. Meza Acevedo, L. Ta and A. Williams for technical assistance; G. Maki for graphics; and G. Howard and K. Claiborne for editorial assistance. The Gladstone Center for In vivo Imaging Research was supported in part by grants from H. Lundbeck A/S, the S.D. Bechtel, Jr. Foundation, and the Conrad N. Hilton Foundation (17348 to K.A.). The microscopy studies were carried out in part at facilities adapted for this project at the National Center for Microscopy and Imaging Research, which is supported by grant P41 GM10341 (awarded to M.H.E.). Gladstone Institutes was supported by NIH/NCRR grant RR18928. The Mouse Pathology Core of the UCSF Helen Diller Family Comprehensive Cancer Center was supported by CA082103. J.K.R., D.D. and A.S.M. were supported by National Multiple Sclerosis Society (NMSS) Postdoctoral Fellowships; J.K.R. and D.D. were supported by Race to Erase MS Young Investigator Awards and American Heart Association (AHA) Scientist Development Grants; V.A.R. was supported by postdoctoral fellowships from AHA and NIH/NINDS F32 NS096920; A.S.M. was supported by NIAID T32AI733429 and NMSS FG-1708-28925; K.K.H. was supported by NSF pre-doctoral fellowship DGE-0648991/1144247; M.A.P. was supported by a NIH/NICHD K12-HD072222; L.M. was supported by a gift from the Dolby Family; S.S.Z. was supported by NIH R01 NS092835; R21 NS108159, NMSS RG1701-26628, RG 5179A10/2, the Weill Institute and the Maisin Foundation; and R.A.S. was supported by NIH R01 NS081149. This work was also supported by grants to K.A. from NMSS (RG3782), H. Lundbeck A/S, the Conrad N. Hilton Foundation (17348), a gift from the Levine Family, and NIH/NINDS (R01 NS052189, R21 NS082976 and R35 NS097976).

Author contributions

J.K.R. performed and designed experiments and analyzed data; V.A.R. did two-photon imaging and AD studies; A.M.-F. and K.K.A. did microglia inhibition experiments; R.A.A., S.L.S. and C.B. did EAE experiments; R.A.A., J.B.S. and R.B.N. produced antibodies; A.M.-F., S.B.P., L.O.P., V.M. and C.B. did antibody-binding ELISA; P.E.R.C. and M.R.M. did histology; K.M.B. did immunohistochemistry and coagulation assays; K.H. and A.R.P. performed the bioinformatics analysis; P.E.R.C., S.B., M.R.M., J.P.C. and M.A.P. did image analysis; A.S.M. performed qPCR array and flow cytometry; D.D. performed EAE studies; I.P. performed immunoblot analysis; S.J.P. and K.K.H. produced recombinant CD11b I domain; C.S., H.H., M.H.E., M.R.A. and R.B.N. analyzed data; R.A.S., S.S.Z., S.H.Z., L.M., and S.B.F. designed experiments; J.B.S. and R.B.N. designed experiments and analyzed data; K.A. conceived of the project, designed the study and analyzed data; and J.K.R. and K.A. wrote the manuscript with input from all authors.

Competing interests

H. Lundbeck A/S sponsored research in K.A.'s laboratory at the Gladstone Institutes. K.A. is a co-founder and scientific advisor of MedaRed and is an inventor on patents US7807645, US8569242, US8877195 and US8980836, covering fibrin antibodies, issued by the University of California. K.A. and J.K.R. are co-inventors on patent US9669112 covering fibrin in vivo models, issued by Gladstone Institutes, and the Gladstone Institutes' pending patent application US20160320370, covering in vitro fibrin assays. K.A., A.M.-F., M.R.A. and K.K.A. are co-inventors on the Gladstone Institutes' and University of California's pending patent application US20170003280, covering assays for inhibition of microglia activation. Their interests are managed by the Gladstone Institutes in accordance with its conflict-of-interest policy. J.B.S., R.B.N., S.B.P., L.O.P., V.M., S.H.Z. were employees of Lundbeck during the time the work was performed.

Additional information

Supplementary information is available for this paper at <https://doi.org/10.1038/s41590-018-0232-x>.

Reprints and permissions information is available at www.nature.com/reprints.

Correspondence and requests for materials should be addressed to K.A.

Publisher's note: Springer Nature remains neutral with regard to jurisdictional claims in published maps and institutional affiliations.

© The Author(s), under exclusive licence to Springer Nature America, Inc. 2018

Methods

Animals. SJL/J mice, C57BL/6 mice, *Cx3cr1^{GFP/+}* mice⁵⁵, *Thy1-YFP* mice (Tg(*Thy1-YFP*)HJrs)⁵⁶, 5XFAD mice (B6SJL-Tg (APPSwF1Lon,PSEN1**M146L**L286V) 6799 Vas/Mmjax)⁵⁷, and mice with genetic ablation of *p47^{phox}* (ref. 58) were purchased from The Jackson Laboratory, and Sprague-Dawley rat P₀ litters were purchased from Charles River Laboratories. 5XFAD mice were crossed with *Thy1-YFP* mice to generate 5XFAD:*Thy1-YFP* mice. *Ccr2^{RFP/RFP}* mice on a C57BL/6 background (provided by I.F. Charo (Gladstone Institutes)) were bred to generate *Cx3cr1^{GFP/+}Ccr2^{RFP/+}* mice⁵⁹. Mice were housed in groups of five under standard vivarium conditions and a 12 h light–12 h dark cycle. All animal protocols were approved by the Committee of Animal Research at the University of California, San Francisco, and were in accordance with the National Institutes of Health guidelines.

Mouse monoclonal antibody production. The synthesis of human fibrinogen peptides $\gamma_{190-202}$ and $\gamma_{377-395}$ and production of mouse monoclonal antibodies were performed by A&G Pharmaceuticals. Screening of 480 hybridomas was performed by ELISA against peptides or the carrier protein. Positive clones were expanded and re-tested to confirm peptide epitope reactivity to either $\gamma_{190-202}$ or $\gamma_{377-395}$. Target candidates were identified as outlined in Supplementary Fig. 1a. The structural map of the γ C domain of fibrinogen was generated using the PyMOL Molecular Graphics System, version 1.6 (Schrödinger) with PDB accession code 1FIC.

Peptide-binding assays. Human peptide $\gamma_{377-395}$ (Genscript) in carbonate buffer (0.1 M NaHCO₃ and 0.15 M NaCl) was coated onto MaxiSorp ELISA plates (Thermo Fisher Scientific) overnight at 4 °C. Wells were incubated with blocking buffer (3% bovine serum albumin (BSA) and 0.1% NP-40 in PBS) for 2 h at 25 °C, washed with 0.05% Tween-20 in PBS. Antibodies 5B8, 4F1, 4E11 and 1E3 were diluted in blocking buffer and were added to the wells for 2 h at 25 °C, followed by secondary polyclonal goat anti-mouse IgG/HRP (#P0447, DAKO) in blocking buffer for 2 h at 25 °C and results were developed with TMB substrate (Sigma-Aldrich) with absorbance at 450 nm measured with an Envision Microplate reader (Perkin Elmer). For competition ELISA, antibody 5B8 was diluted to 2 nM in blocking buffer and was pre-incubated with increasing concentrations of human or mouse peptide $\gamma_{377-395}$ and $\gamma_{190-202}$ for 3 h at 25 °C. Competition of 5B8 with $\gamma_{377-395}$ or $\gamma_{190-202}$ was assessed by incubation on plates coated with human peptide $\gamma_{377-395}$.

Fibrin or fibrinogen binding. Human plasminogen-free fibrinogen (#341578, EMD Millipore) was depleted of IgG with a Pierce albumin/IgG removal kit (Thermo Fisher Scientific). IgG-depleted human plasminogen-free fibrinogen (25 μ g/ml) in 20 mM HEPES buffer, pH 7.4, was treated with 0.3 U/ml bovine thrombin (Sigma-Aldrich) and 7 mM CaCl₂ in MaxiSorp ELISA plates (Thermo Fisher Scientific) for 1.5 h at 37 °C. Formed fibrin was dried onto the wells at 37 °C overnight. IgG-depleted human fibrinogen (25 μ g/ml) was coated onto the wells at 37 °C for 2.5 h. Plates were washed with binding buffer (10 mM HEPES, pH 7.4, 150 mM NaCl, 3 mM EDTA and 0.05% Tween-20) and were incubated with blocking buffer (binding buffer containing 3% BSA) for 1 h at 25 °C. Monoclonal antibodies in blocking buffer were incubated for 1 h at 25 °C. Following washing with binding buffer, polyclonal goat anti-mouse IgG/HRP (#P0447, DAKO) in blocking buffer was added for 1 h at 25 °C, and the signal was developed with Lumi-Phos HRP (Lumigen) and measured with an Envision Microplate reader. Experiments of antibody binding to peptides, fibrin and fibrinogen performed at the Gladstone Institutes were independently reproduced at the UCSF Small Molecule Discovery Center and at Lundbeck, US with similar results.

CD11b I-domain production. Plasmid pET15-His-TEV-CD11b was constructed by cloning of the CD11b I-domain (residues Q130-S326) into a pET15b-derived plasmid at the NdeI and XhoI sites, preceded by an N-terminal 6xHis tag and followed by a TEV protease cleavage site (pET15-His-TEV-CD11b), then was transformed into Rosetta2(DE3) cells. Protein was expressed and purified as described⁶⁰, with the exception that cells were lysed by a pressure-driven microfluidizer, and His-containing proteins were trapped using TALON cobalt affinity resin. Protein purity was assessed to be >90% by LC-MS and gel electrophoresis.

CD11b I-domain ELISA. 96-well ELISA plates (Greiner) were coated with 25 μ g/ml fibrin or fibrinogen and were incubated in blocking buffer as indicated for binding assays for 1 h before the addition of 50 μ l per well of biotinylated CD11b I-domain in PBS with 0.5% BSA and 0.05% Tween-20 for 2 h at 37 °C, followed by incubation with 1 μ g/ml HRP-coupled streptavidin (BD Pharmingen, 1:1,000) for 1 h at 25 °C and were developed by incubation with TMB/E substrate (Chemicon-Millipore), and absorbance was measured at 450 nm with a Synergy H4 plate reader (BioTek). For 5B8 competition ELISA, after incubation in blocking buffer, 5B8 was diluted at twofold concentrations from 0.02 μ M to 10 μ M and was incubated for 2 h at 37 °C, followed by incubation of 6.88 μ M CD11b I-domain for 2 h at 25 °C.

Cell culture. Primary microglia and BMDMs were isolated, cultured and treated with fibrin or LPS as previously described¹⁶. PBMCs (AllCells) (2×10^6 cells/ml) were plated in RPMI-1640 medium supplemented with 10% heat-inactivated FBS, 1% penicillin-streptomycin and 50 ng/ml human M-CSF (#300–25, Peprotech)

in tissue-culture-treated dishes (Corning). After 24 h, non-adherent cells were removed, and adherent cells were cultivated for an additional 7–8 d at 37 °C in 5% CO₂.

Morphometry. Primary microglia were stimulated with fibrin for 48 h as described¹⁶. Microglia were fixed with 4% PFA, permeabilized with 0.1% Triton X-100 and immunostained with FITC-labeled Isolectin B4 (1:300; Sigma-Aldrich) and/or CellMask Red Stain (Thermo Scientific). Blocking involved pre-incubation with 80 μ g/ml antibodies or mouse IgG2b (clone MPC-11, BioXCell BE0086, distributed by the UCSF Monoclonal Antibody Core, endotoxin concentrations < 0.002 EU/ μ g) or IgG2b (eBiosciences, endotoxin level < 0.01 EU/ μ g) for 2 h at 37 °C before plating of cells for a final concentration of antibodies at 40 μ g/ml. For manual analysis, images were collected using an Axioplan 2 Zeiss microscope with an Axiocam HRC camera and analyzed using ImageJ. 250 cells per condition were counted for each experiment. Activated microglia were classified on the basis of a surface area of >2,000 μ m². For automated image acquisition and analysis, images of microglia cells were acquired with the GEHC IN-Cell Analyzer 2000, using a 10 \times lens and excitation/emission filter pairs of 350 nm/455 nm (CellMask Red Stain) and 579 nm/624 nm (Hoechst dye). Images were analyzed with the GEHC IN-Cell Developer Toolbox version 1.9. The Hoechst-stained nuclei were segmented using a 'nuclear' segmentation type, with a set minimum target area of 30 μ m² and a set sensitivity of 75%. To minimize artifacts, segmentation with less than 120 intensity units or area greater than 1,000 μ m² were excluded. The CellMask Red-stained whole microglia cells were segmented using an 'intensity' segmentation type, with a set threshold between 200 intensity units and 4095 intensity units. The borders of adjacent contacting cells were resolved using the 'clump breaking' segmentation post-processing, which utilizes discrete nuclei as seeds. For segmentation by size, cells > 800 μ m² were classified as activated microglia. Only cells containing a nucleus within the cell body area were accepted. All segmented nuclei and cells were then recorded as individual counts.

Fibrin polymerization assay. Human fibrinogen was diluted to 0.15 mg/ml in 20 mM HEPES (pH 7.4) containing 0.15 M NaCl and 5 mM ϵ -amino caproic acid and was combined with 0.3 U/ml thrombin (Sigma-Aldrich), and 10 mM CaCl₂. Antibodies (50 μ g/ml) or GPRP peptide (Bachem) were incubated with fibrinogen for 2 h at 37 °C before mixture with CaCl₂-thrombin. Absorbance at 350 nm over intervals of 60 s was measured using a SpectraMax M5 microplate reader (Molecular Devices) with SoftMax Pro 5.2 software (Phoenix Technologies).

Plasma clotting time and aPTT assay. Plasma-clotting times were measured as described¹³ by combination of equal volumes of citrated plasma and 2 U/ml bovine thrombin (Enzyme Research Laboratories) and 40 mM CaCl₂ at 37 °C. The aPTT assay was performed with pooled normal human plasma (Innovative Research) using 50 μ g/ml 5B8 or IgG2b or 0.5 mM GPRP peptide (Bachem). Plasma was incubated with 5B8 or IgG2b at 37 °C for 2 h. Clotting was initiated by aPTT-XL (Ellagic acid activator) and 0.02 M CaCl₂ (Thermo Fisher Scientific) and was monitored at 405 nm in a SpectraMax M5 microplate reader.

Real time qPCR, multi-plex qPCR and microarray analysis. RNA isolation, real-time PCR and microarray analysis were performed as described¹⁶. Primers are listed in Supplementary Table 3. Microarray data from GEO accession code GSE71084 were used to select ROS-encoding genes with significant expression (log₂ values) to generate heat maps for primary microglia and BMDMs. For multiplex qPCR, primary microglia were plated in 96-well black μ -clear-bottomed microtiter plates (Greiner Bio-One) in DMEM, 10% FBS, 1% penicillin-streptomycin and were allowed to adhere for 24 h before being treated for 4 h with 1 μ M fibrin D-dimer (HyTest) as described¹². 5B8 or IgG2b (each 20 μ g/ml) was pre-incubated with fibrin D-dimer in DMEM for 3 h at 37 °C before cell treatment. Gene expression was assessed using the RT2 Profiler PCR Array (Rat Inflammatory & Autoimmunity; Qiagen), and only differentially expressed genes (a difference in expression of over twofold; $P < 0.05$) were reported as the 'mean fold change'. Experiments analyzing the inhibition of gene expression by antibodies performed at the Gladstone Institutes were independently reproduced at Lundbeck, US with similar results.

Oxidant detection with DHE. BMDMs or PBMCs were incubated in RPMI containing 5 μ M DHE (Invitrogen) for 30 min. 100,000 cells/well were plated on 96-well black μ -clear-bottomed microtiter plates (Greiner Bio-One) pre-coated with 25 μ g/ml fibrin. 5B8 or IgG2b (each 20 μ g/ml) (UCSF Monoclonal Antibody Core clone LTF-2) was added in fibrin-coated wells 2 h before plating of cells. BMDMs were incubated with 300 μ M apocynin (Calbiochem) for 1 h or 5 μ g/ml of anti-CD11b (M1/70, eBioscience) for 30 min before plating. Cells were incubated on fibrin for 24–48 h and were fixed with 4% PFA for 10 min, and DHE fluorescence was detected at 518 nm/605 nm using a SpectraMax M5 microplate reader. Cells were quantified by DAPI counterstaining. In mice, in vivo administration of DHE and detection were performed as described¹⁵.

NADPH-oxidase activity. BMDMs were plated on 25 μ g/ml fibrin-coated six-well plates (Greiner Bio-One). 5B8 or IgG2b (each 20 μ g/ml) was added to the

fibrin plates 2 h before plating cells. NADPH-oxidase activity was assayed by the lucigenin-enhanced chemiluminescence method⁴¹. Cells were collected with a cell scraper and were homogenized in ice-cold Krebs buffer, pH 7.4 (119 mM NaCl, 2.5 mM KCl, 1 mM NaH₂PO₄, 1.3 mM MgCl₂, 2.5 mM CaCl₂, 11 mM glucose and 20 mM HEPES, pH 7.4). The cell homogenate was centrifuged at 1,000g, and the pellet was resuspended with luminescence buffer (Krebs buffer containing 10 μM lucigenin; Cayman Chemicals), before the addition of 100 μM NADPH substrate (Sigma-Aldrich). Luminescence was detected by an EnSpire microplate reader.

Immunoblots. BMDMs cultured on plates coated with 25 μg/ml fibrin were lysed in RIPA lysis buffer (EMD Millipore) with protease-phosphatase inhibitor cocktail (EMD Millipore). Protein extracts (20 μg) were separated by electrophoresis on NuPAGE 4–12% Bis-Tris Gel (Life Technologies) and were transferred onto nitrocellulose. Blots were blocked in 5% milk in TBST and were incubated with antibody to gp91^{phox} (1:1,000; clone EPR6991, Abcam), phosphorylated p40^{phox} (1:1,000; Thr154, Cell Signaling Technology) or GAPDH (1:5,000; clone 14C10, Cell Signaling Technology), followed by horseradish peroxidase-conjugated secondary antibody (1:5,000; Cell Signaling Technology #7074S) and an enhanced chemiluminescence (ECL) kit (GE Healthcare) for detection. Densitometry analysis was performed using ImageJ.

Cortical neuron–macrophage co-culture. Cortices from P₁ rats were finely minced and were digested for 30 min at 37 °C in DPBS (Gibco) containing papain (Worthington Biochemicals) and DNase (Sigma-Aldrich). Papain was inhibited by the addition of ovomucoid (Worthington Biochemicals). Neurons were plated at a density of 60,000 cells/cm² on poly-D-lysine–pre-coated eight-well Permanox chamber slides (Sigma-Aldrich) in Neurobasal/B27 medium (Invitrogen) and were cultured for 10 d. Rat BMDMs were cultured in RPMI-1640 with 10% heat-inactivated FBS (Invitrogen), 1% penicillin-streptomycin (Corning), and 10 ng/ml rat M-CSF (#400–28, Peprotec). BMDMs were plated on 25 μg/ml fibrin-coated plates with 20 μg/ml 5B8 or IgG2b for 24 h and were lifted with PBS–EDTA as described¹⁶, then were added to cortical neuron cultures for 2 d, fixed with 4% PFA and immunostained with anti-MAP-2 (1:1,000; clone AP20, EMD Millipore); thresholded images were quantified with the NeurphologyJ plug-in in ImageJ. 2.5 × 10¹⁰ GC/ml of AAV1.hSyn.TurboRFP (University of Pennsylvania Vector Core) was used to transduce primary cortical neurons for 8 d before the addition of fibrin-stimulated BMDMs for 12 h. RFP images were thresholded and the neurite fragments were analyzed using the ImageJ plugin 'Analyze Particles'. Quantification was performed by an observer blinded to experimental treatment.

Pharmacokinetics. C57BL/6 mice were given intraperitoneal injection of 400 μg 5B8. Blood samples were collected by micro-accusampler and were centrifuged at 2,500 r.p.m. for 15 min. Plasma was stored at –80 °C until analysis. Plasma was diluted 1:1,000 in blocking buffer (3% BSA and 0.1% NP-40 in PBS). 5B8 was diluted in blocking buffer to create a concentration curve. Plasma and 5B8 were added to wells coated with human peptide γ_{377–395} and were incubated for 2 h at 25 °C. After washing, polyclonal goat anti-mouse IgG–HRP (#P0447, DAKO) in blocking buffer was added for 2 h at 25 °C, and the assay was developed with TMB Liquid substrate (Sigma-Aldrich), with absorbance measured using an Envision Microplate reader.

EAE. EAE was induced in 8- to 9-week-old female SJL/J mice, C57BL/6 mice or *Cx3cr1*^{GFP/+}*Ccr2*^{RFP/+} mice by subcutaneous immunization with 100 μg PLP_{139–151} (HSLGKWLGHDPDKF; Auspep) or 50 μg MOG_{35–55} (MEVGWYRSPFSRVVHLYRDKG; Auspep) in complete Freund's adjuvant (Sigma-Aldrich) supplemented with 400 μg of heat-inactivated *Mycobacterium tuberculosis* H37Ra (Difco Laboratories). 2 d after immunization, mice were given intraperitoneal injection of 200 ng (C57BL/6) or 75 ng (SJL/J) pertussis toxin (Sigma-Aldrich). For adoptive transfer, donor SJL/J mice were immunized as described above, and on day 10, cells from the draining lymph nodes and spleen were isolated. Lymphocytes were re-stimulated with 20 μg/ml PLP_{139–151} nd 10 ng/ml of IL-12 (eBioscience) for 4 d, and 3 × 10⁷ cells were transferred into healthy SJL/J recipient mice. The frequency of donor CD4⁺ T cells producing IFN-γ was assessed by flow cytometry before transfer. For prophylactic treatment, mice were each given 800 μg of either 5B8 or isotype-matched control antibody IgG2b every 2 d from day 0. For therapeutic treatment, antibodies were injected every 2 d starting at the peak of the initial paralytic episode. Mice were observed daily, and clinical scores were assigned as follows by observers blinded to treatment: 0, no symptoms; 1, loss of tail tone; 2, ataxia; 3, hindlimb paralysis; 4, hindlimb and forelimb paralysis; 5, moribund.

Histology and immunohistochemistry. For histological analysis, spinal cords and brains were processed as described^{3,15}. Antibodies used were as follows: mouse antibody to non-phosphorylated neurofilament H (1:100; BioLegend clone SMI-32), rabbit anti-Iba-1 (1:1,000; Wako #019–19741) and mouse anti-myelin basic protein (1:100; BioLegend clone SMI-99) and Alexa Fluor 488 or 594 (1:500; Jackson ImmunoResearch) for detection. Immunohistochemistry for anti-MBP was performed with the Mouse on Mouse (M.O.M.) kit (Vector Labs). *Cx3cr1*^{GFP/+}*Ccr2*^{RFP/+} mice were perfused with 4% PFA and spinal cord

segments were frozen in OCT, then cut into 10-μm sections and stained with DAPI for 5 min. DHE labeling was performed as described¹⁵. For analysis of 5XFAD mice, mice were perfused with 4% PFA and brains were post-fixed in 4% PFA overnight at 4 °C, except for CD11b staining, for which they were post-fixed for 4 h immunohistochemistry in coronal brain sections (30 μm) were performed using antibodies to ChAT (1:1,000, EMD Millipore #AB144P), CD11b (1:150; eBioscience clone M1/70), Iba-1 (1:1,000; Wako), MAC-2 (1:1,000; Cedarlane clone M3/38), fibrinogen (1:1,000; J. L. Degen, Cincinnati Children's Hospital Medical Center), and human Aβ (1:500; IBL-America #18584). Amyloid plaques were labeled with methoxy-XO4 (fluorescent probe for Aβ, Tocris) as described⁶². Images were acquired with an Axioplan II epifluorescence microscope (Zeiss) equipped with dry Plan-Neofluar objectives (10× and 0.3 NA, 20× and 0.5 NA, or 40× and 0.75 NA) or an all-in-one BZ-X700 fluorescence microscope (Keyence) or a Fluoview FV1000 (Olympus) confocal microscope and FluoView Software v3.1b. Excitation lasers were set to 405 nm, 488 nm and 543 nm, and Olympus 20× and 1.00 NA, Olympus 25× and 1.05 NA, or an Olympus 40× and 0.8 NA water-immersion lens with 1.0 μm z-step and Kalman filtering using line mode of 2 were used. Quantification of Iba1, Aβ, MAC-2⁺ was averaged from nine field of views of high Aβ plaque density throughout the cortex. Images were quantified using ImageJ by observers blinded to experimental conditions.

Flow cytometry. Primary mouse splenocytes were isolated from 5B8- or IgG2b-treated mice 10 d after immunization with PLP_{139–151}. Cell suspensions were stained with combinations of antibodies to the following: CD45 (BioLegend clone 30-F11), CD3 (BioLegend clone 17A2), CD4 (BioLegend clone GK1.5), CD11b (BioLegend clone M1/70), B220 (BD Bioscience clone RA3-6B2), Ly6G (eBioscience clone RB6-8C5) and CD11c (BioLegend clone NA18). For cytokine analysis, cells were incubated for 4 h with Cell Activation Cocktail (BioLegend), and surfaces were stained for CD3, CD4 and CD8 (BioLegend clone 53-6.7). Cells were then fixed with Cytofix/Cytoperm solution (BD Biosciences), and intracellular cytokine staining was performed with anti-IFN-γ (BioLegend clone XMG1.2) and anti-IL-17-FITC (BioLegend clone TC11-18H10.1). All antibodies were used at 1:300. Flow cytometry was performed on an LSR II (BD Biosciences). Data were analyzed using FlowJo (Tree Star).

Stereotactic fibrinogen injection and drug treatment. Stereotactic injection of fibrinogen into the corpus callosum of *Cx3cr1*^{GFP/+} or C57BL/6 mice and analysis were performed as described^{15,16}. 5B8, 5B8-F(ab) fragment or isotype-matched control antibody IgG2b (clone MPC-11, eBioscience) was injected (10 μg at 0.2 μl/min) into the cerebral ventricle (AP, –2.0 mm; ML, 0 mm; DV, –2.0 mm) with a 10 μl syringe attached to a 33-gauge needle 30 min before fibrinogen injection.

5B8 penetration in the CNS and target engagement. Mice were given intraperitoneal injection of 800 μg/mouse of biotinylated 5B8 every 2 d (three total doses). Mice were perfused with saline, and the spinal cord or brain was processed for fresh frozen sections as described¹³. Sections were fixed with 4% PFA for 10 min, and biotinylated 5B8 was detected using Cy3-conjugated streptavidin (1:100; Invitrogen) for 30 min at 25 °C. Sections were incubated for 1 h with antibody to fibrinogen (1:2,000), followed by FITC donkey anti-rabbit (1:500; Jackson ImmunoResearch) for 30 min at 25 °C. For amyloid plaque staining, sections were counterstained with Methoxy-XO4 (Tocris; 4% vol of 10 mg/ml).

Two-photon in vivo imaging. *Thy1*-YFP and *Thy1*-YFP:5XFAD mice were given intravenous injection of Alexa594-conjugated fibrinogen (Invitrogen) daily for 3 d as described¹⁵. Mice were also given intraperitoneal injection of Methoxy-XO4 24 h before imaging. Methoxy-XO4 was solubilized with DMSO–propylene glycol–PBS pH 7.5 (ratio, 2:9:9) at 5 mg/ml. On the day of imaging, a small craniotomy was made, and a custom-made metal plate was affixed to a stage to stabilize the skull. Alexa594–fibrinogen solution was injected retro-orbitally before imaging. The anesthetized animal was placed on a heated pad under an Ultima-IV multiphoton microscope (Prairie) equipped with MaiTai DeepSee-eHP lasers (Spectra Physics). The excitation wavelength was 820 nm to simultaneously visualize fibrinogen, methoxy-XO4 and YFP dendrites. Imaging was performed from 20 to 150 μm below the dura, using a Nikon 40× and 0.8 NA immersion lenses with a 1.0 μm z-step. z-stacks of images were projected along the z-axis to recreate two-dimensional representations of the 3D structures within the imaged volumes. Images were adjusted for brightness, contrast and background noise with ImageJ. Spectral unmixing plugin in ImageJ was used to separate overlapping signals.

Network analyses. The TYROBP network and the Microglia Pathogen Phagocytosis Pathway were 'translated' from human-specific, static figures to mouse-specific data models using WikiPathways⁶³ and HomoloGene. The co-expression network was constructed by extraction of the dominant cluster of downregulated genes of interest (selected from those with change in expression of –0.5-fold or less (log₂ values) and raw *P* value of <0.05) on the basis of co-expression interaction data provided by GeneMANIA⁶⁴. Subsequent network visualization, layout, data overlays and subnetwork extraction were performed in Cytoscape⁶⁵.

Statistical analyses. Data are presented as mean \pm s.e.m. Statistical calculations were performed with GraphPad Prism (Version 6.03). Sample sizes were based on previous experiments and were not predetermined by statistical methods. Statistical significance was determined with a non-parametric two-sided Mann-Whitney test, Kruskal-Wallis test, Welch's two-sample *t*-test, or one-way or two-way analysis of variance followed by Bonferroni or Tukey's post-test (multiple comparisons). Linear models were fitted for each gene using the Bioconductor 'limma' package in R⁶⁶. Moderated *t*-statistics, change in expression ('fold' values) and the associated *P* values were calculated for each gene. Mice were randomly assigned to experimental groups for EAE and 5XFAD experiments. The assignment of scores for EAE in mice was performed in a blinded fashion. All animals survived to the end of the study, and all data points were included in analysis. All histopathological analysis and quantification was performed in a blinded way.

To compare clinical scores for EAE, the linear mixed-effects models were performed using the R statistical package. Means of maximum clinical scores were compared using a two-sample *t*-test as implemented in R using the Welch's *t*-test and the Wilcoxon rank sum test. *P* values were corrected for multiple testing using the Holm procedure. The statistical significance of the changes in the mean clinical score for each day of the experiment was estimated using permutation tests. The corresponding *P* values were estimated using 1,000 permutations in all prophylactic antibody treatment and 10,000 permutations for therapeutic antibody treatment. In each permutation, mice were randomly permuted. To compare the first day of onset, the log-rank test was used as implemented by the 'survdiff' function in the 'survival' package in R.

Reporting Summary. Further information on research design is available in the Nature Research Reporting Summary linked to this article.

Data availability

GEO data supporting the findings of this study have been deposited in the GEO depository under accession numbers [GSE118920](https://www.ncbi.nlm.nih.gov/geo/query/acc.cgi?acc=GSE118920) and [GSE118921](https://www.ncbi.nlm.nih.gov/geo/query/acc.cgi?acc=GSE118921). Networks are permanently referenced in two Wikipathways entries: TYROBP Causal Network (*Mus musculus*) (<http://www.wikipathways.org/index.php?title=Pathway:WP3625&oldid=85694>) and Microglia Pathogen Phagocytosis Pathway (*Mus musculus*) (<http://www.wikipathways.org/index.php?title=Pathway:WP3626&oldid=85691>). The authors declare that all other data

supporting the findings of this study are available within the paper. Any additional data can be made available from the corresponding author upon request.

References

- Jung, S. et al. Analysis of fractalkine receptor CX(3)CR1 function by targeted deletion and green fluorescent protein reporter gene insertion. *Mol. Cell. Biol.* **20**, 4106–4114 (2000). Medline.
- Feng, G. et al. Imaging neuronal subsets in transgenic mice expressing multiple spectral variants of GFP. *Neuron* **28**, 41–51 (2000).
- Oakley, H. et al. Intraneuronal β -amyloid aggregates, neurodegeneration, and neuron loss in transgenic mice with five familial Alzheimer's disease mutations: potential factors in amyloid plaque formation. *J. Neurosci.* **26**, 10129–10140 (2006).
- Jackson, S. H., Gallin, J. I. & Holland, S. M. The p47phox mouse knock-out model of chronic granulomatous disease. *J. Exp. Med.* **182**, 751–758 (1995).
- Saederup, N. et al. Selective chemokine receptor usage by central nervous system myeloid cells in CCR2-red fluorescent protein knock-in mice. *PLoS One* **5**, e13693 (2010).
- Jensen, M. R. et al. Structural basis for simvastatin competitive antagonism of complement receptor 3. *J. Biol. Chem.* **291**, 16963–16976 (2016).
- Abid, M. R., Spokes, K. C., Shih, S. C. & Aird, W. C. NADPH oxidase activity selectively modulates vascular endothelial growth factor signaling pathways. *J. Biol. Chem.* **282**, 35373–35385 (2007).
- Klunk, W. E. et al. Imaging Abeta plaques in living transgenic mice with multiphoton microscopy and methoxy-X04, a systemically administered Congo red derivative. *J. Neuropathol. Exp. Neurol.* **61**, 797–805 (2002).
- Kutmon, M. et al. WikiPathways: capturing the full diversity of pathway knowledge. *Nucleic Acids Res.* **44**, D488–494 (2016).
- Warde-Farley, D. et al. The GeneMANIA prediction server: biological network integration for gene prioritization and predicting gene function. *Nucleic Acids Res.* **38**, W214–220 (2010).
- Shannon, P. et al. Cytoscape: a software environment for integrated models of biomolecular interaction networks. *Genome Res.* **13**, 2498–2504 (2003).
- Gentleman, R. C. et al. Bioconductor: open software development for computational biology and bioinformatics. *Genome Biol.* **5**, R80 (2004).

Reporting Summary

Nature Research wishes to improve the reproducibility of the work that we publish. This form provides structure for consistency and transparency in reporting. For further information on Nature Research policies, see [Authors & Referees](#) and the [Editorial Policy Checklist](#).

Statistical parameters

When statistical analyses are reported, confirm that the following items are present in the relevant location (e.g. figure legend, table legend, main text, or Methods section).

n/a Confirmed

- The exact sample size (n) for each experimental group/condition, given as a discrete number and unit of measurement
- An indication of whether measurements were taken from distinct samples or whether the same sample was measured repeatedly
- The statistical test(s) used AND whether they are one- or two-sided
Only common tests should be described solely by name; describe more complex techniques in the Methods section.
- A description of all covariates tested
- A description of any assumptions or corrections, such as tests of normality and adjustment for multiple comparisons
- A full description of the statistics including central tendency (e.g. means) or other basic estimates (e.g. regression coefficient) AND variation (e.g. standard deviation) or associated estimates of uncertainty (e.g. confidence intervals)
- For null hypothesis testing, the test statistic (e.g. F , t , r) with confidence intervals, effect sizes, degrees of freedom and P value noted
Give P values as exact values whenever suitable.
- For Bayesian analysis, information on the choice of priors and Markov chain Monte Carlo settings
- For hierarchical and complex designs, identification of the appropriate level for tests and full reporting of outcomes
- Estimates of effect sizes (e.g. Cohen's d , Pearson's r), indicating how they were calculated
- Clearly defined error bars
State explicitly what error bars represent (e.g. SD, SE, CI)

Our web collection on [statistics for biologists](#) may be useful.

Software and code

Policy information about [availability of computer code](#)

Data collection

Fibrin clotting was traced by measuring absorbance at 350nm over intervals of 60 s using a SpectraMax M5 microplate reader (Molecular Devices) with SoftMax Pro 5.2 software (Phoenix Technologies Ltd.). qPCR data were collected on the StepOnePlus™ Real-Time PCR System (ThermoFisher Scientific). Flow cytometry data were acquired on a BD LSR II (BD Biosciences) with BD FACSDiva™ software. Confocal microscopy images were taken using a Fluoview FV1000 (Olympus) confocal microscope and Fluoview Software. Immunohistochemical microscopy images were collected on an Axioplan II epifluorescence microscope (Zeiss). Two-photon in vivo imaging data were acquired on an Ultima-IV multiphoton microscope (Prairie) equipped with MaiTai DeeSee-eHP lasers (Spectra Physics). The PyMOL Molecular Graphics System, Version 1.6 Schrödinger, LLC was used for the structural map of the γ C-domain of fibrinogen.

Data analysis

GraphPad Prism software v7.03 (GraphPad Software, Inc.) was used to prepare graphs and to perform statistical analyses. Automated Image acquisition and Analysis: Images of microglia cells were acquired with the GEHC IN-Cell Analyzer 2000™ and analyzed with the GEHC IN-Cell Developer Toolbox version 1.9. Multiplex qPCR for primary rat microglia: Array analysis was performed with the online RT2 Profiler Data Analysis Software following manufacturer's default setting (<http://pcrdataanalysis.sabiosciences.com/pcr/arrayanalysis.php>). Fold change was calculated based on the comparative delta delta Ct method and statistical significance was determined by Student's t -test. Differentially expressed genes were deemed when fold change was >2 and $p < 0.05$. Flow cytometry data were analyzed using FlowJo software (Tree Star, Inc.). MAP-2+ neurite area was quantified with the NeurphologyJ software plug-in to skeletonize the entire well images. Resulting images were thresholded and area was measured with NIH ImageJ analysis software (v1.50). Fluorescent images of primary neurons expressing RFP were thresholded and the degree of fragmentation (number of fragments) was analyzed using the ImageJ plugin 'Analyze Particles.' The statistical test for the differential expression that informed the network figure data overlays: Linear

models were fitted for each gene using the Bioconductor ‘limma’ package in R. Moderated t-statistics, fold change and the associated P values were calculated for each gene. The coexpression network was constructed by extracting the dominant cluster of downregulated genes of interest (selected from those with log₂ fold change of -0.5 or less and raw p-value < 0.05) based on coexpression interaction data provided by GeneMANIA. Subsequent network visualization, layout, data overlays and subnetwork extraction were performed in Cytoscape. Two classes of statistical tests were used to test for differences in the variation of clinical scores and time of onset in the four EAE models between treatment groups. To compare EAE clinical scores, the linear mixed effects models were first performed using the R statistical package. The comparison of means of maximum clinical scores was performed using a two-sample t-test as implemented in R using the Welch’s t-test and the Wilcoxon rank sum test. P-values were corrected for multiple testing using the Holm procedure. The statistical significance of the changes in the mean clinical score for each day of the experiment was estimated using permutation tests. The corresponding p-values were estimated using 1000 permutations in all prophylactic antibody treatment and 10000 permutations for therapeutic antibody treatment. In each permutation, mice were randomly permuted. To compare the first day of onset, the log-rank test was used as implemented by the survdiff function in the survival package in R.

For manuscripts utilizing custom algorithms or software that are central to the research but not yet described in published literature, software must be made available to editors/reviewers upon request. We strongly encourage code deposition in a community repository (e.g. GitHub). See the Nature Research [guidelines for submitting code & software](#) for further information.

Data

Policy information about [availability of data](#)

All manuscripts must include a [data availability statement](#). This statement should provide the following information, where applicable:

- Accession codes, unique identifiers, or web links for publicly available datasets
- A list of figures that have associated raw data
- A description of any restrictions on data availability

GEO data supporting the findings of this study have been deposited in the GEO depository under accession numbers GSE118920 and GSE118921.

The TYROBP network and the Microglia Pathogen Phagocytosis Pathway were translated from human-specific, static figures to mouse-specific data models using WikiPathways and HomoloGene, and are permanently referenced by these links, respectively: <http://wikipathways.org/index.php?title=Pathway:WP3625&oldid=85694>, <http://wikipathways.org/index.php?title=Pathway:WP3626&oldid=85691>.

The authors declare that all other data supporting the findings of this study are available within the paper. Any additional data can be made available from the corresponding author upon request.

Field-specific reporting

Please select the best fit for your research. If you are not sure, read the appropriate sections before making your selection.

Life sciences Behavioural & social sciences Ecological, evolutionary & environmental sciences

For a reference copy of the document with all sections, see [nature.com/authors/policies/ReportingSummary-flat.pdf](https://www.nature.com/authors/policies/ReportingSummary-flat.pdf)

Life sciences study design

All studies must disclose on these points even when the disclosure is negative.

Sample size	No statistical methods were used to predetermine sample size, but our sample sizes are similar to those reported previously.
Data exclusions	No samples or animals were excluded from the analysis. For the microglia morphology assay, an exclusion criterion applied was fibrin-induced activation < 20 % compared to control . Experiments with activation > 20% were used for analysis.
Replication	Experiments were replicated several times with reproducible results, as indicated in each figure legend. Fibrin antibody binding to peptides, fibrin, and fibrinogen and gene expression antibody inhibition experiments performed at the Gladstone Institutes were all independently validated at Lundbeck, US with similar results. Fibrin antibody binding studies performed at the Gladstone Institutes were also independently validated at the University of California, San Francisco Small Molecule Discovery Center with similar results.
Randomization	Animals were randomly assigned to experimental groups at the beginning of experiments. The randomization of animal studies is stated in the Methods section.
Blinding	For EAE studies and histopathological experiments, the researchers were blinded as to the mouse treatment conditions. Mice were scored by blinded observers. Mice were divided into experimental groups in an unbiased manner. The mice were randomized and coded to assign groups or collect data for animal experiments. A set of the binding, morphology and fibrin polymerization assays of the monoclonal fibrin antibodies were performed in a blinded manner and the code was unblinded at the end of all three experimental assays. All imaging of immunohistology and quantification experiments were performed in a blinded manner.

Reporting for specific materials, systems and methods

Materials & experimental systems

n/a	Involvement	Involved in the study
<input type="checkbox"/>	<input checked="" type="checkbox"/>	Unique biological materials
<input type="checkbox"/>	<input checked="" type="checkbox"/>	Antibodies
<input checked="" type="checkbox"/>	<input type="checkbox"/>	Eukaryotic cell lines
<input checked="" type="checkbox"/>	<input type="checkbox"/>	Palaeontology
<input type="checkbox"/>	<input checked="" type="checkbox"/>	Animals and other organisms
<input checked="" type="checkbox"/>	<input type="checkbox"/>	Human research participants

Methods

n/a	Involvement	Involved in the study
<input checked="" type="checkbox"/>	<input type="checkbox"/>	ChIP-seq
<input type="checkbox"/>	<input checked="" type="checkbox"/>	Flow cytometry
<input checked="" type="checkbox"/>	<input type="checkbox"/>	MRI-based neuroimaging

Unique biological materials

Policy information about [availability of materials](#)

Obtaining unique materials

Distribution of antibodies to non-profit investigators will be under a Material Transfer Agreement (MTA) where applicable. A request for reimbursement of expenses for shipping and handling, and other costs associated with production and delivering materials to the requesting investigator where applicable.

Antibodies

Antibodies used

gp91phox (clone EPR6991, Abcam), Phospho-p40phox (clone Thr154, Cell Signaling Technology), GAPDH (clone 14C10, Cell Signaling Technology), Horseradish peroxidase-conjugated secondary antibody (catalog#7074S, Cell Signaling Technology), MAP-2 (clone AP20, EMD Millipore), neurofilament H non-phosphorylated (clone SMI-32, Biolegend), Iba-1 (catalog# 019-19741, Wako), myelin basic protein (clone SMI-99, Biolegend), choline acetyltransferase (catalog# AB144P, EMD Millipore), CD11b (clone M1/70, eBioscience), Mac-2 (clone M3/38, Cedarlane), fibrinogen (kind gift of Dr. Jay Degen), human amyloid beta (catalog# 18584, IBL-America), CD45 (clone 30-F11, Biolegend), CD3 (clone 17A2, Biolegend), CD4 (clone GK1.5, Biolegend), CD11b (clone M1/70, Biolegend), B220 (clone RA3-6B2, BD Bioscience), Ly6G (clone RB6-8C5, eBioscience), and CD11c (clone N418, Biolegend), anti-IFN- γ (clone XMG1.2, Biolegend) and anti-IL-17-FITC (clone TC11-18H10.1, Biolegend), polyclonal goat anti-mouse IgG-HRP (catalog# P0447, DAKO), Purified mouse IgG2b isotype control (clone MPC-11, UCSF Monoclonal Antibody Core), and Purified Rat IgG2b isotype control (clone LTF-2, UCSF Monoclonal Antibody Core).

Validation

All antibodies used in this study are from commercial sources and have been validated by the vendors. Validation data are available on the manufacturer's website. Appropriate antibody dilutions were performed based on preliminary experiments and intensity of fluorescent signals.

Animals and other organisms

Policy information about [studies involving animals](#); [ARRIVE guidelines](#) recommended for reporting animal research

Laboratory animals

SJL/J, C57BL/6, Cx3cr1GFP/+, Thy1-YFP (Tg(Thy1-YFP)HJrs), 5XFAD (B6SJL-Tg (APPSwF1Lon,PSEN1*M146L*L286V) 6799 Vas/Mmjax), and p47phox^{-/-} mice were purchased from The Jackson Laboratory. 5XFAD were crossed with Thy1-YFP to generate 5XFAD:Thy1-YFP mice. Mothers and their newborn Sprague-Dawley rats (P0) were purchased from Charles River Laboratories. Ccr2RFP/RFP on a C57BL/6 background were bred to generate Cx3cr1GFP/+Ccr2RFP/+ mice. Microglia were prepared from neonatal rat pups at postnatal day (P) 2–3. Bone marrow cells were isolated from tibia and femur of 10-week-old C57BL/6 mice. Active experimental autoimmune encephalomyelitis (EAE) was induced in 8–9-week-old female SJL/J, C57BL/6, or Cx3cr1GFP/+Ccr2RFP/+ mice. Both male and female 5XFAD mice were used.

Wild animals

The study did not involve wild animals.

Field-collected samples

The study did not involve samples collected from the field.

Plots

Confirm that:

- The axis labels state the marker and fluorochrome used (e.g. CD4-FITC).
- The axis scales are clearly visible. Include numbers along axes only for bottom left plot of group (a 'group' is an analysis of identical markers).
- All plots are contour plots with outliers or pseudocolor plots.
- A numerical value for number of cells or percentage (with statistics) is provided.

Methodology

Sample preparation

Primary splenocytes were harvested and processed for flow cytometric analysis as described in Methods. Supplementary Fig 6. Cells were harvested, stained for surface antigens, fixed and then immediately analyzed by LSR II (BD Biosciences. Supplementary Fig 6b. For cytokine recall analysis, cells were incubated for 4 h with Cell Activation Cocktail (Biolegend) in vitro prior to surface and intracellular antigen staining, and then analyzed via LSR II (BD Biosciences)

Instrument

LSR II (BD)

Software

BD FACSDiva and FlowJo software v10

Cell population abundance

When cells were sorted or enriched, the purity was confirmed by flow cytometry and routinely >95 %.

Gating strategy

Lymphocytes were gated by FSC-A/SSC-A and then doublet discrimination was performed first by FSC-H/FSC-W followed by SSC-H/SSC-W. Next, CD45-negative cells were gated out and then gating strategy focused on quantifying cell specific populations based on the following definitions: CD45+CD3+CD8+ T cells; CD45+CD3+CD4+ T cells; CD45+CD3+CD4+IL17+ and CD45+CD3+CD4+IFN γ + T cells; CD45+CD3-B220+ B cells; CD45+CD11b+Ly6G+ neutrophils; CD45+CD11b+CD11c+ dendritic cells; CD45+CD11b+CD11b-Ly6g- myeloid cells

- Tick this box to confirm that a figure exemplifying the gating strategy is provided in the Supplementary Information.